Dynamics of Simulated High-Shear, Low-CAPE Supercells

ANDREW R. WADE[a] AND MATTHEW D. PARKER[a]

[a] *Department of Marine, Earth, and Atmospheric Sciences, North Carolina State University, Raleigh, North Carolina*

(Manuscript received 27 April 2020, in final form 25 December 2020)

ABSTRACT: High-shear, low-CAPE environments prevalent in the southeastern United States account for a large fraction of tornadoes and pose challenges for operational meteorologists. Yet, existing knowledge of supercell dynamics, particularly in the context of cloud-resolving modeling, is dominated by moderate- to high-CAPE environments typical of the Great Plains. This study applies high-resolution modeling to clarify the behavior of supercells in the more poorly understood low-CAPE environments, and compares them to a benchmark simulation in a higher-CAPE environment. Simulated low-CAPE supercells' main updrafts do not approach the theoretical equilibrium level; their largest vertical velocities result not from buoyancy, but from dynamic accelerations associated with low-level mesocyclones and vortices. Surprisingly, low-CAPE tornado-like vortex parcels also sometimes stop ascending near the vortex top instead of carrying large vorticity upward into the midlevel updraft, contributing to vortex shallowness. Each of these low-CAPE behaviors is attributed to dynamic perturbation pressure gradient accelerations that are maximized in low levels, which predominate when the buoyancy is small.

KEYWORDS: Mesocyclones; Severe storms; Supercells; Tornadoes; Convective storms

1. Introduction

a. *High-shear, low-CAPE convection*

Severe convective storms in environments with little convective available potential energy (CAPE) and large vertical wind shear pose a combination of hazards to life and property. High-shear, low-CAPE (HSLC) environments can produce significant severe weather. Nearly half of all tornadoes in the United States occur with mixed-layer CAPE (MLCAPE) less than 1000 J kg^{-1}, and 16% of significant (F/EF2+) tornadoes occur with MLCAPE less than 500 J kg^{-1} (Schneider and Dean 2008). [Definitions of HSLC environments vary. For this study, we use the looser upper limit of 1000 J kg^{-1} MLCAPE, and the Sherburn et al. (2016) shear criterion of at least 18 m s^{-1} 0–6-km bulk wind difference]. Forecast, watch, and warning skill is diminished in HSLC episodes. This parameter space accounts for a disproportionate fraction of tornado watch false alarm hours (Dean and Schneider 2008), and tornado warning verification statistics deteriorate as CAPE decreases (Anderson-Frey et al. 2016). Even though the violent (F/EF4+) tornadoes responsible for most tornado deaths (Ashley 2007) tend to occur with CAPE greater than 1000 J kg^{-1} (Cohen 2010), improving HSLC watches and warnings remains crucial because of their frequency and the possible influence of their performance on public response across all environments (Simmons and Sutter 2009; Ripberger et al. 2014). Furthermore, HSLC events are most common in the Southeast (Guyer et al. 2006; Schneider et al. 2006; Sherburn and Parker 2014), where both meteorological and nonmeteorological vulnerabilities make tornadoes more likely to take lives (e.g., Ashley 2007).

There are several meteorological causes of reduced skill at all lead times in HSLC events. The CAPE-dependent significant tornado parameter (STP; Thompson et al. 2003) is typically below its established threshold of 1 in southeastern HSLC severe events (Sherburn and Parker 2014). Similarly, Anderson-Frey et al. (2018) showed that even though STP is much lower in the Southeast in winter than in spring, about the same proportion of tornadoes reach EF2+ intensity. HSLC environments that produce severe weather often destabilize on time and space scales poorly represented by the observing network and some forecast models (King et al. 2017). Furthermore, the sensitivity of small CAPE and large low-level shear to planetary boundary layer (PBL) parameterizations (Cohen et al. 2015, 2017) in operational weather models adds to the difficulty of anticipating and diagnosing HSLC severe risks. Limitations of operational weather radar detection are a primary cause of the HSLC tornado warning problem. In HSLC events, tornadic and nontornadic radial velocity signatures are indistinguishable beyond about 60 km from a WSR-88D (Davis and Parker 2014) because of their width and height relative to the radar beam. The convective mode climatology of Smith et al. (2012) showed that although quasi-linear convective systems (QLCSs) produce a larger share of tornadoes in the Southeast than in the Great Plains, supercells (Browning 1964) are still the storm mode of most concern in every region, responsible for 88% of significant tornadoes nationwide. The present study focuses exclusively on supercells.

Studies of buoyancy-limited supercells (e.g., Markowski and Straka 2000; Davies 2006) have usually found lower storm tops than those occurring with large CAPE. Some note narrower horizontal dimensions as well (Kennedy et al. 1993). These smaller storms are often termed "miniature supercells," particularly but not exclusively in the context of landfalling tropical cyclone tornadoes (McCaul 1991). Storm-scale dynamics

Supplemental information related to this paper is available at the Journals Online website: https://doi.org/10.1175/JAS-D-20-0117.1.s1.

Wade's current affiliation: Cooperative Institute for Mesoscale Meteorological Studies, University of Oklahoma, Norman, Oklahoma.

Corresponding author: Andrew Wade, arwade@ncsu.edu

DOI: 10.1175/JAS-D-20-0117.1

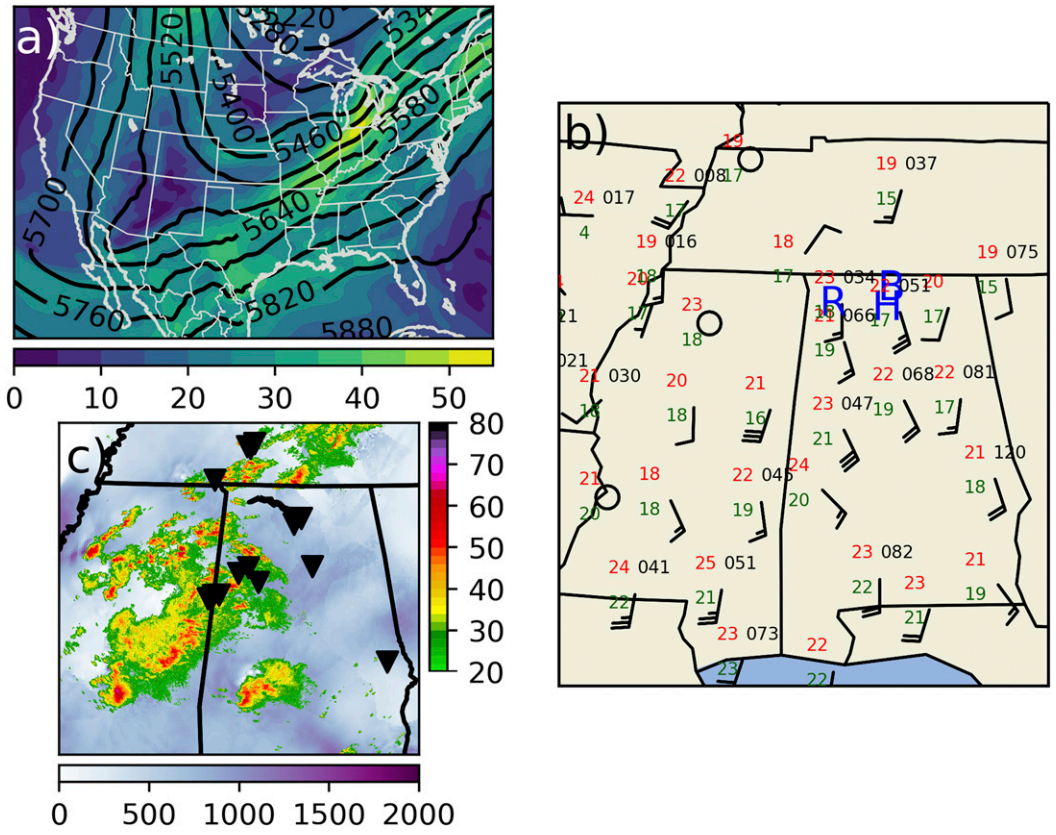

FIG. 1. The 0000 UTC 1 Apr 2016 (a) observed 500-hPa height (contoured every 60 m) and wind speed ($m\,s^{-1}$); (b) selected surface observations, with the Alabama locations of Belle Mina, Russellville, and Hartselle denoted by their initials in blue; and (c) lowest-tilt radar reflectivity (dBZ) for the three WSR-88Ds in the VORTEX-SE domain, HRRR analysis MLCAPE (J kg^{-1}), and event tornado reports (triangles).

of HSLC supercells are sparsely studied compared to higher-CAPE supercells. McCaul and Weisman (1996) simulated an idealized mini-supercell associated with a landfalling tropical cyclone, an environment that technically qualifies as HSLC despite shear and humidity profiles that may be quite different from a cool-season warm sector. This study demonstrated that the dynamic vertical perturbation pressure gradient acceleration (VPPGA) dominates buoyancy in such a mini-supercell. Subsequent simulations (McCaul and Weisman 2001) also showed that the vertical distribution of buoyancy modulates storm intensity more strongly in low-CAPE environments. More recently, Sherburn and Parker (2019) simulated mixed-mode HSLC convection ahead of an artificial cold front, with supercell structures often embedded in linear segments. This design highlighted both the environmental dependencies described above and the dominance of the nonlinear dynamic VPPGA in enhancing low-level updrafts and stretching near-ground vertical vorticity into strong vortices.

To the authors' knowledge, high-quality observations of HSLC supercells' three- or four-dimensional structure (i.e., multi-Doppler analyses using mobile radars) do not exist. Murphy and Knupp (2013) used a single operational WSR-88D for a synthetic dual-Doppler analysis of two cool-season southeastern supercells that happened to pass very near the radar in a quasi–steady state. Their analysis found an updraft maximum at a low altitude (~3 km) forced primarily by dynamic VPPGA, and little to no rear-flank downdraft (RFD). They specifically noted the difficulty of targeting southeastern supercells with multiple radars.

b. *Open questions*

Some recent high-resolution simulations of tornadic supercells (e.g., Orf et al. 2017) have mentioned extension of these techniques to environments beyond their typical Great Plains high-CAPE base states. Sherburn and Parker (2019) called for higher-resolution modeling to explain "how HSLC vortices differ from those in higher-CAPE convection." The radar climatology of Davis and Parker (2014) also recommended modeling studies to clarify the differences between high- and low-CAPE vortices, particularly the shallowness of HSLC radar signatures. In some of the observational works cited above, low-CAPE storms' overall shallowness results from a low equilibrium level (EL). There is not such a clear physical reason for low-CAPE vortices to be shallower. It seems plausible that vortex depth is simply a matter of scaling with a lower-topped storm beneath a lower cool-season tropopause and EL—the same essential kinematics and dynamics compressed into a shallower layer. It is not obvious why a parent supercell

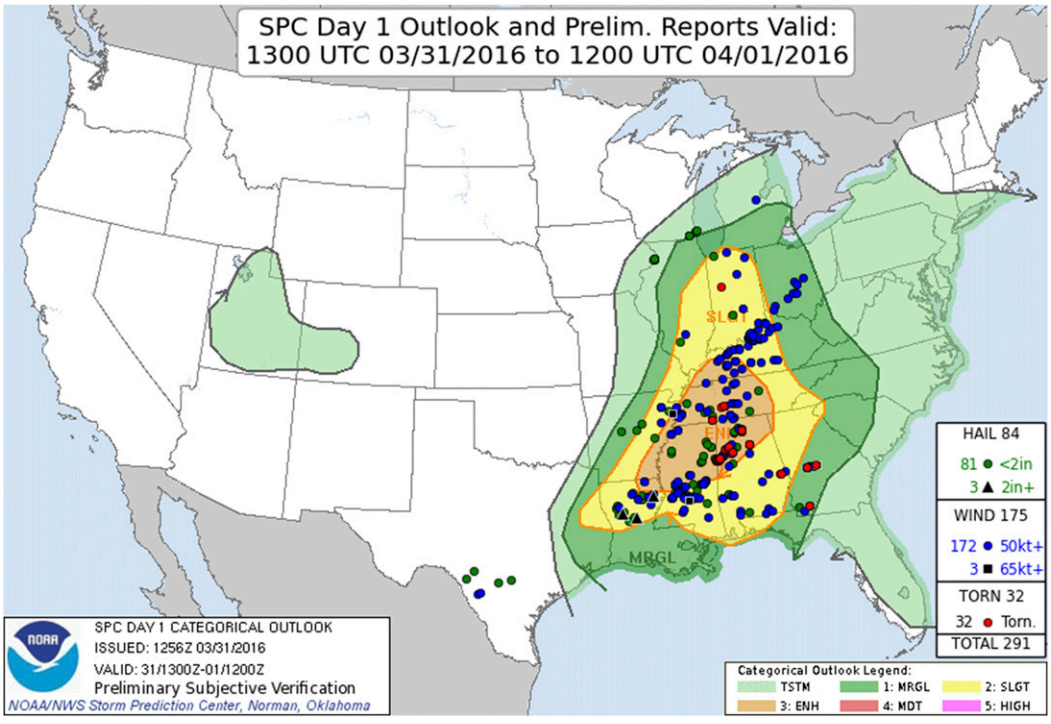

FIG. 2. Storm Prediction Center convective outlook issued at 1300 UTC 31 Mar 2016, with storm reports from the forecast period overlaid.

with updraft depth >5 km would produce a vortex that remains shallow enough to inhibit radar detection (i.e., 1–2 km). Does vortex behavior have an unexplored relationship to the buoyancy profile (being only incidentally correlated to storm depth)? What are the roles of buoyancy and dynamic VPPGA in driving supercell updrafts and vortices under varying CAPE? To what extent can dynamic effects compensate for limited buoyancy? To explore the possible dynamical differences between low- and high-CAPE storms, we use southeastern environments to simulate one tornadic supercell with moderate to high CAPE and three others with low CAPE.

2. 31 March 2016 severe event

While the idealized simulations are not meant to replicate a specific observed storm, the low-CAPE runs use base states drawn from the 31 March 2016 severe event during the Verification of the Origins of Rotation in Tornadoes Experiment–Southeast (VORTEX-SE). A positively tilted trough with its axis from the upper Midwest through New Mexico and Arizona dominated the upper-level synoptic pattern across the contiguous United States (Fig. 1a). Broad west-southwesterly flow aloft overlay the VORTEX-SE domain throughout the day. 500-hPa winds exceeded 20 m s^{-1} over most of the Southeast. Ahead of the trough axis, a ~992-hPa surface low moved northeastward across Michigan and Lake Huron. Its attendant cold front trailed from the Great Lakes into the lower Mississippi Valley. A moist warm sector overspread the VORTEX-SE domain ahead of the front (Fig. 1b). In the morning of 31 March an expansive complex of stratiform rain and nonsevere thunderstorms covered much of the warm sector, but this precipitation weakened and exited the domain to the east from 1600 to 1800 UTC. Thunderstorms that began just ahead of the cold front entered the domain from the west and additional discrete supercells formed in the open warm sector (Fig. 1c). Several supercell tornadoes (triangles in Fig. 1c) occurred near the Alabama–Mississippi border during this early evening phase. During the evening, storm mode gradually evolved from quasi-discrete supercells to supercell

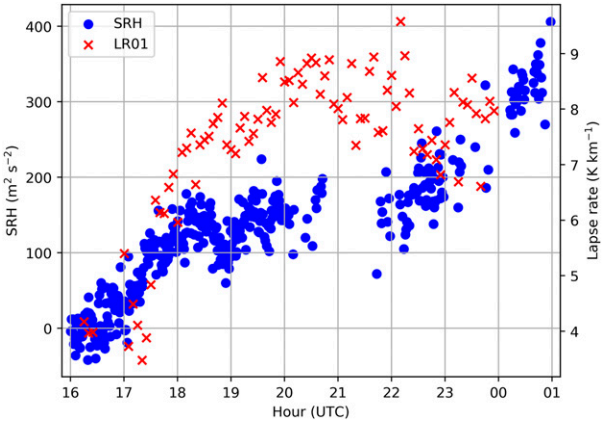

FIG. 3. SRH and lapse rate in the 0–1 km AGL layer observed by CLAMPS at Belle Mina, AL, on 31 Mar and 1 Apr 2016.

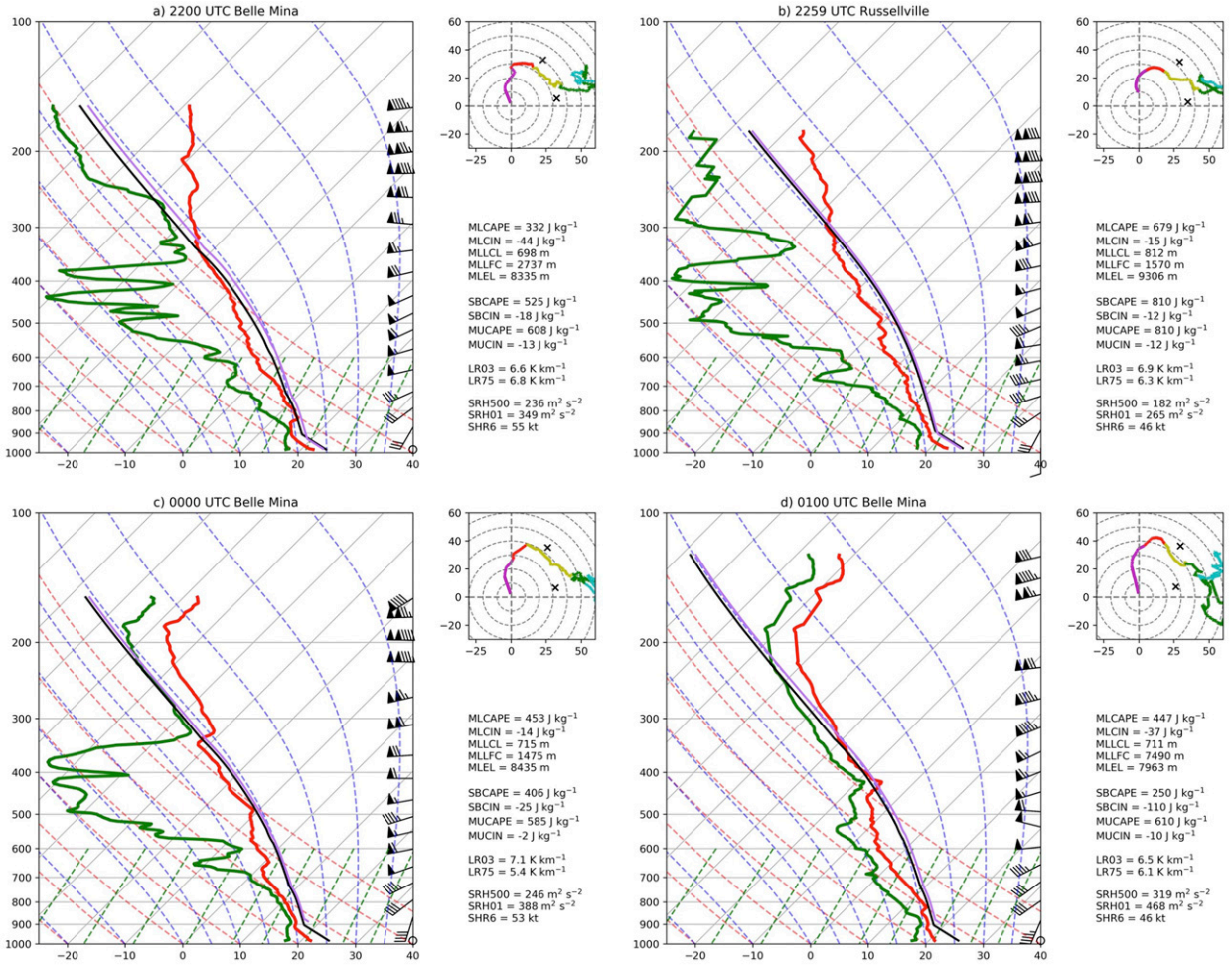

FIG. 4. VORTEX-SE observed soundings at (a) Belle Mina, AL, at 2200 UTC 31 Mar 2016; (b) Russellville, AL, at 2259 UTC 31 Mar 2016; (c) Belle Mina, AL, at 0000 UTC 1 Apr 2016; and (d) Belle Mina, AL, at 0100 UTC 1 Apr 2016. Hodograph changes color at 0.5, 1, 3, and 6 km, and × denotes left and right Bunkers storm motion.

clusters embedded in stratiform rain. Such cells later produced two more tornadoes between 0100 and 0300 UTC in north-central Alabama, including an EF2 near Hartselle. Despite the difficulties of HSLC forecasting detailed above, the Storm Prediction Center day 1 convective outlook (Fig. 2) anticipated this event well.

The Collaborative Lower Atmospheric Mobile Profiling System [CLAMPS; Wagner et al. (2019)] captured the evolution of the planetary boundary layer near Belle Mina in north-central Alabama during most of this event. CLAMPS observed a sharply increasing 0–1-km lapse rate as the PBL rapidly destabilized in the wake of the morning precipitation (Fig. 3). Though 0–1-km shear magnitude (not shown) was maximized before destabilization, 0–1-km storm-relative helicity (SRH, calculated using observed motion of storms later in the evening) increased in the late morning and early afternoon, and again in the early evening. This trend suggests strong synoptic influences on the wind profile, since diurnal mixing typically acts to reduce SRH in the PBL; the two opposing effects appear to have roughly canceled during the 1900–2200 UTC window when SRH was steady. VORTEX-SE soundings also captured a range of convective environments, ranging from over 1000 J kg^{-1} MLCAPE during the afternoon in western parts of the domain to much lower CAPE in northern Alabama late in the evening; Fig. 4 shows the evolution of northern Alabama profiles from 2200 to 0100 UTC. By 0030 UTC, CLAMPS was sampling over 300 m^2 s^{-2} 0–1-km SRH in northern Alabama. One profile exceeded 400 m^2 s^{-2} at 0100 UTC (Fig. 3).

One curiosity among the dense VORTEX-SE observations is the lack of strong surface outflow (cold pools). Figure 5 depicts changes in near-surface temperature and moisture associated with the passage of radar-observed precipitation features during the 31 March 2016 severe event in the Southeast. Temperature perturbations are modest (only a few degrees Celsius) and not clearly linked to the organization or intensity of attendant precipitation structures. The closest surface station to the center of an intense discrete cell, Texas Tech "stesonet" site 0215A, experienced a drop of 2–3 K with a sudden temporary rebound. The most pronounced drop (~4 K

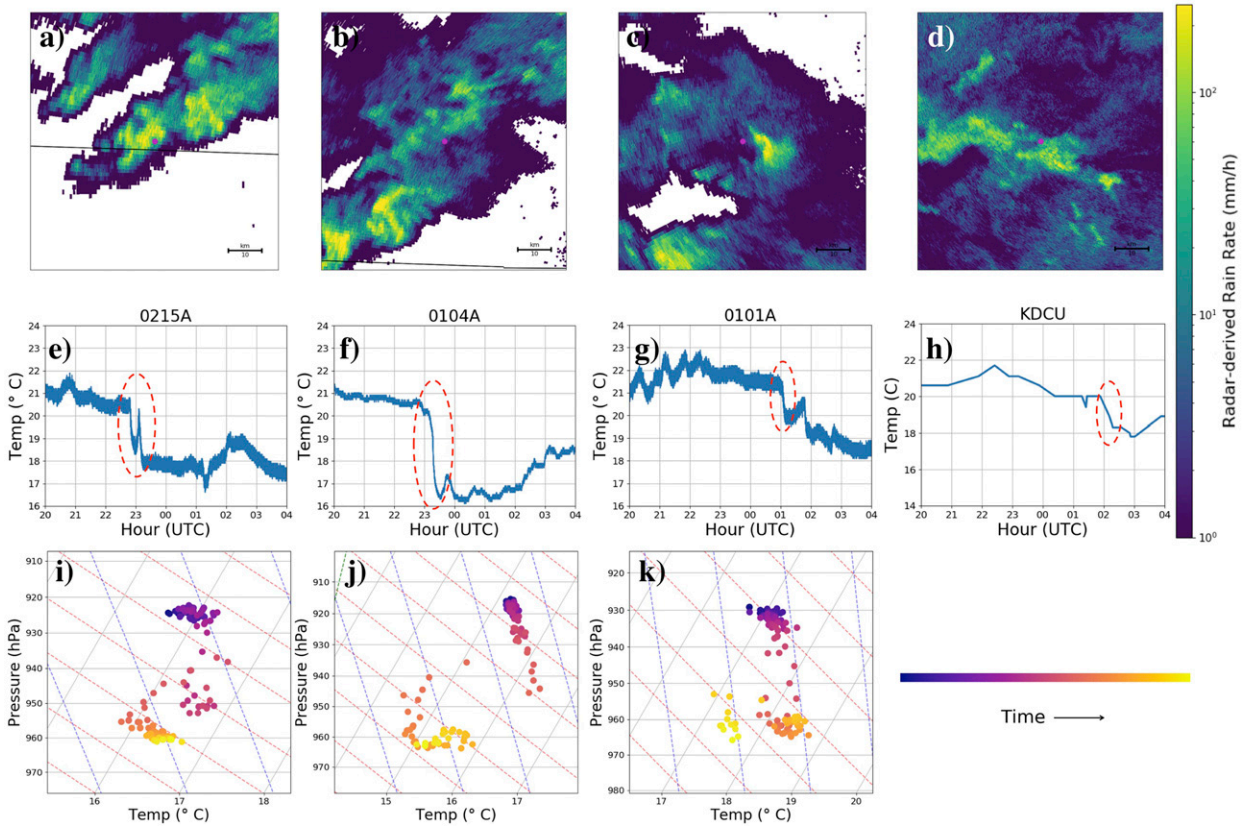

FIG. 5. (a)–(d) Radar-derived rain rate (mm h^{-1}) at lowest tilt from the nearest WSR-88D as surface stations (magenta dots at center) experience sudden temperature drops; (e)–(h) temperature time series corresponding to the above radar images, with the time of interest circled; and (i)–(k) saturation points on zoomed skew T–log$p$ diagrams spanning 2 h of evolution from inflow to outflow in the above time series.

at site 0104A) was associated with a far less organized area of stratiform and weakly convective rain. In general, saturation points (Betts 1984) at the selected stesonet sites (Figs. 5i–k) over 2-h periods from the prestorm inflow to the coldest outflow initially descended along a moist adiabat comparably to Betts (1984) before abruptly jumping to a distinct, colder outflow airmass, suggesting horizontal heterogeneity of outflow with different source regions. This pattern is present to some extent at all

TABLE 1. Key model settings for idealized supercell simulations.

Model option	Setting	Notes
Horizontal grid length	100 m	
Lowest scalar level	10 m AGL	Stretched vertical grid
Vertical levels	84	94 for high-CAPE
Domain size	144 km × 144 km × 18.2 km	21.2 km for high-CAPE
Time step	Adaptive	
Lower boundary	Free-slip	See discussion
Lateral boundaries	Open-radiative	
Upper boundary	Rigid lid	
Rayleigh damping	$\alpha = 0.0033$	Near model lid and sides
Microphysics	Mansell et al. (2010)	See discussion
CCN concentration	2.0×10^9 cm^{-3}	
Graupel, hail collection efficiency	0.75	
Subgrid turbulence	TKE/Deardorff	
PBL	Not parameterized	Large-eddy simulation
Radiation	Not included	
Surface fluxes	Not included	
Coriolis	Not included	
Storm initiation	Updraft nudging	Naylor and Gilmore (2012)

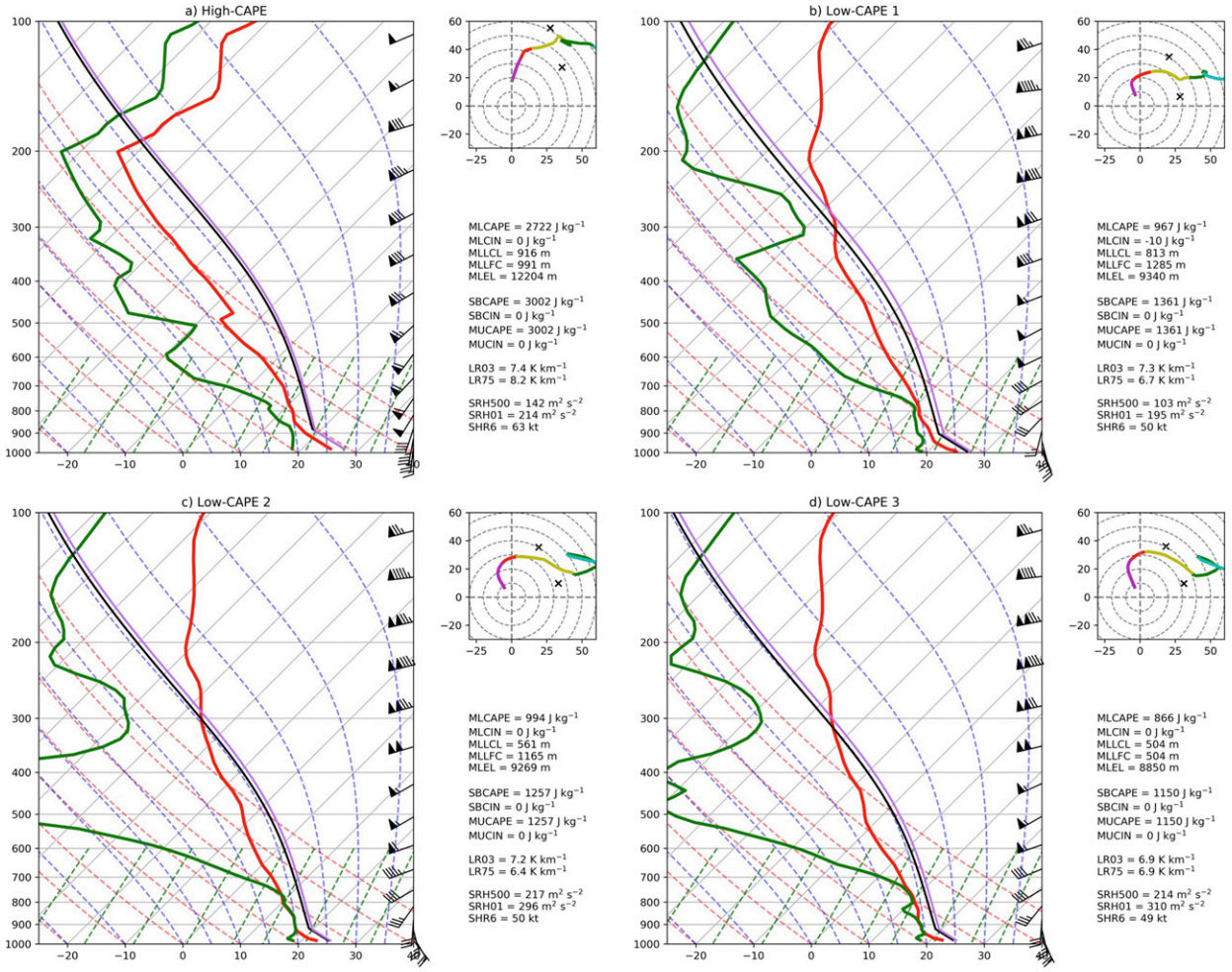

FIG. 6. Skew T–log$p$ diagrams as in Fig. 4 showing base-state profiles and relevant parameters for the four simulations: (a) high-CAPE, (b) low-CAPE 1, (c) low-CAPE 2, and (d) low-CAPE 3.

three stesonet sites but is seen most easily at 0104A (Fig. 5j). For the purposes of this article, these cold pool observations help validate our choice of model configurations, described below.

3. Methods

a. *Model design and configuration*

Like other historical observations of HSLC events, the 31 March 2016 VORTEX-SE dataset stops short of detailed kinematic information about individual storms. Idealized cloud-resolving modeling can fill part of this gap, having been widely used since the 1970s and 1980s to establish supercells' basic internal dynamics and their relationships to parameters of the near-storm environment (e.g., Klemp and Wilhelmson 1978; Rotunno and Klemp 1982, 1985; Weisman and Klemp 1982, 1984). The simulations in this article use Cloud Model 1 (CM1; Bryan and Fritsch 2002) release 19.4, a nonhydrostatic model designed for idealized simulations of thunderstorms. Artificial updraft forcing initiates deep convection in an otherwise horizontally homogeneous environment. Table 1 lists relevant model settings. The effects of microphysics parameterizations and lower boundary conditions are discussed further in the appendix. In short, separate classes for graupel and hail are the safest choice for HSLC environments, and attempting to represent friction systematically inhibits development of large vertical vorticity at the surface in these environments. Surface fluxes, radiative transfer, and Coriolis acceleration are neglected. A horizontal grid length of 100 m is chosen to resolve many aspects of the convection while remaining affordable enough to facilitate multiple simulations. However, it cannot resolve the details of flow within actual tornadoes. Surveyed damage paths in the 31 March 2016 event were as narrow as 200 m at the widest point (NWS Birmingham 2016). So in the convention of similar modeling studies, we refer to "tornado-like vortices" or simply "vortices" rather than tornadoes in these simulations. Furthermore, because of both limited resolution and the free-slip lower boundary condition, near-ground wind speeds do not reliably represent vortex intensity.

Each simulation also contains a large array of parcel trajectories initialized at low levels in the inflow and immediate

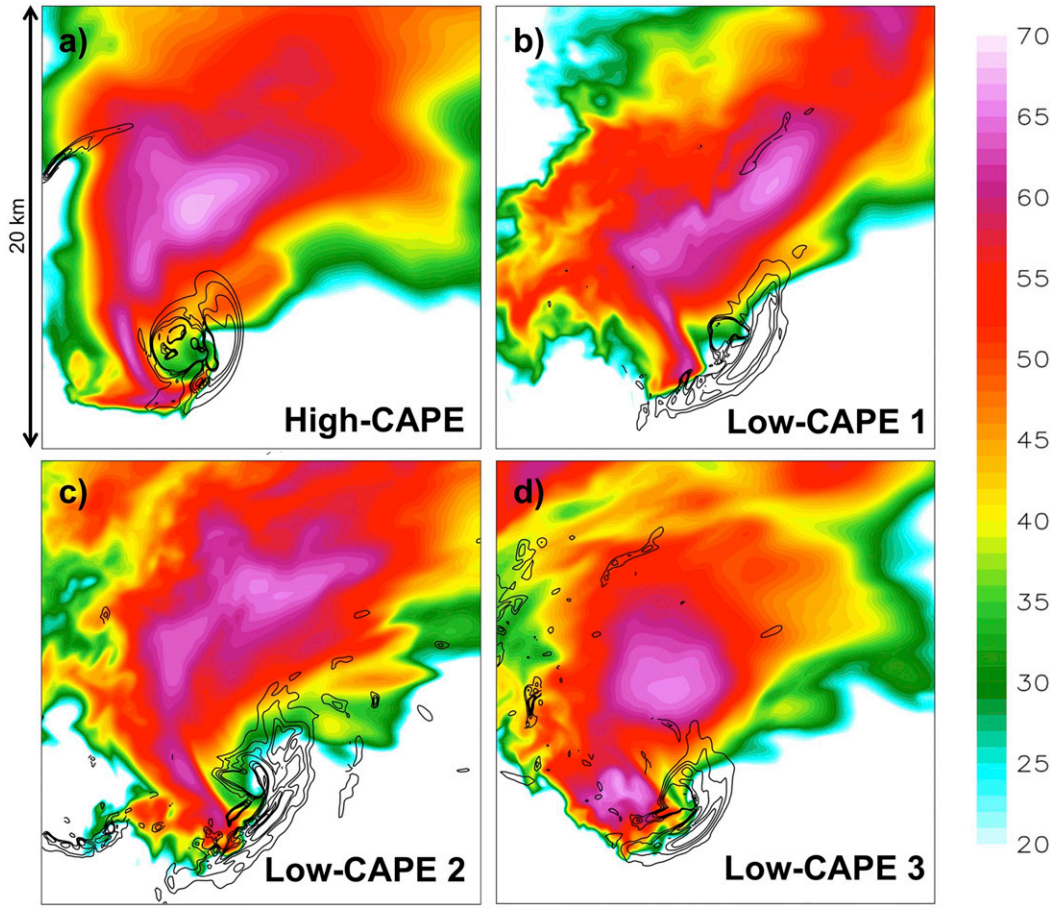

FIG. 7. Simulated reflectivity (dBZ; color fill) at 10 m AGL and 0–3-km updraft helicity ($m\,s^{-2}$; black contours) for all four simulations during tornado-like vortex production. (a) The high-CAPE storm is shown at 89 min of simulation time and (b)–(d) the low-CAPE storms are all shown between 100 and 110 min.

outflow regions, integrated forward during the model runs on the native timesteps. These trajectories are intended to represent the vertical accelerations of updraft parcels near storms' peak intensity and organization, and of vortex parcels near or shortly after the time of vortex formation. In final runs of each simulation, parcels passing through low-level vorticity maxima were reinitialized with "stencils" of six neighbor parcels 0.5 m away on all sides. This was done to enable future work isolating vorticity origins by the method of Dahl et al. (2014). While that analysis is beyond the scope of this paper, many of the added neighbor parcels also qualify as updraft or vortex parcels. They are included in these results with the caveat that they may add less information than parcels in the sparser original network, since they are initialized so close together. Additionally, all parcels passing below the 10-m lowest model level are excluded. In some instances this greatly reduces the number of parcels in the features of interest, but avoids unrealistic parcel behavior below the lowest interior level [e.g., Dahl et al. (2014), section 3b].

b. *Idealized model base states*

Only a fraction of VORTEX-SE soundings from the 31 March 2016 event sampled supportive convective environments. Preliminary idealized simulations (not shown) used some of these as base states. Few sustained intense storms, and those that did were extraordinarily sensitive to small changes in the model setup. Trial and error revealed that some High-Resolution Rapid Refresh [HRRR; Smith et al. (2008)] model analysis profiles had similar convective parameters but served as more reliable base states. Balloon-borne sondes' inability to capture an instantaneous or purely vertical profile is likely problematic in high-shear environments where the corridor of instability is quite narrow and transient (e.g., King et al. 2017). Still, the observed soundings offer qualitative reassurance that the HRRR contains realistic CAPE and shear. They also corroborate the HRRR's steep near-surface lapse rates and large SRH across much of the Alabama warm sector. Ten HRRR analysis profiles were tested as base states. Of the 10, 3 profiles that produced supercells persisting longer than 90 min after the end of artificial forcing were chosen for production runs and detailed analysis. These base states are plotted in Figs. 6b–d.

These three most successful profiles were drawn from a small region of the undisturbed warm sector in the HRRR analysis near the Alabama–Mississippi border (see supplemental figure). While it is not the intent of the idealized study

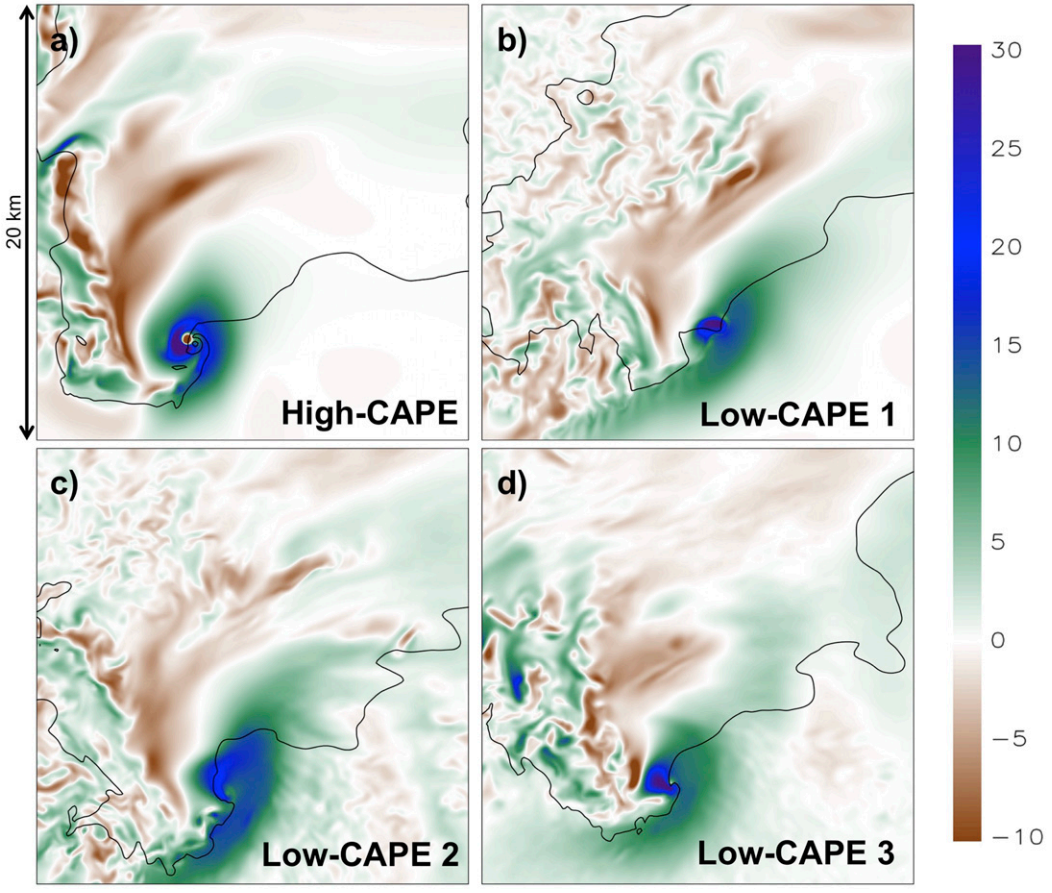

FIG. 8. Vertical velocity (m s^{-1}) at 1 km AGL and simulated reflectivity (30 dBZ contour) at 10 m AGL for all four simulations at the same times as in Fig. 7.

to reproduce a specific storm, both these base states and the idealized design producing discrete tornadic supercells most closely align with the 2300–0000 UTC evolution near the Alabama–Mississippi border. The base states are not representative of some other parts of this event, such as the earlier tornadic supercell in southern Tennessee in modified remnant outflow or the later tornadic supercell in northern Alabama embedded in stratiform rain. The small variations in CAPE and deep shear among these profiles are not expected to result in systematic differences in storm behavior; rather, these are meant to represent a realistic range of discrete supercell behaviors within the evening environment of the 31 March 2016 event. Much more complicated mixed modes [such as some simulated by Sherburn and Parker (2019)] are important in many southeastern events, including later periods of this event, but given the dearth of recent low-CAPE supercell modeling at this resolution, these simulations examine the simplest scenario.

The main difference between these base states and the observed soundings in Fig. 4 is slightly higher CAPE owing to the HRRR profiles' southwestward displacement from the sounding locations (and the balloons' horizontal drift, as noted above). Yet simulating storms with much lower CAPE proved nearly impossible within a horizontally homogeneous base state. Sherburn et al. (2016) and King et al. (2017) highlighted processes like synoptic ascent, potential instability release, and rapid warm/moist advection in HSLC events. All of these processes require horizontal heterogeneity. Their absence in the idealized framework probably explains simulated storms' failure to mature with lower CAPE. Regardless, even at the upper limit of "low CAPE," clear distinctions from higher-CAPE storms will be shown.

Although simulations of higher-CAPE supercells abound in the literature, a higher-CAPE control run in this particular model configuration with the same set of parameterizations is necessary for direct comparison to the HSLC simulations. A historic case was chosen as the base state: the 1800 UTC 3 April 1974 Nashville, Tennessee, sounding (Fig. 6a) in the midst of the Super Outbreak (e.g., Hoxit and Chappell 1975). This very unstable (2722 J kg^{-1} MLCAPE), highly sheared, uncapped profile amid a strongly synoptically forced event is meant to represent the upper end of southeastern tornado environments. Both the 1974 and 2016 profiles contain large vertical shear; this suits the overall aim of these simulations to highlight the effects of varying CAPE, not shear, within realistic southeastern environments.

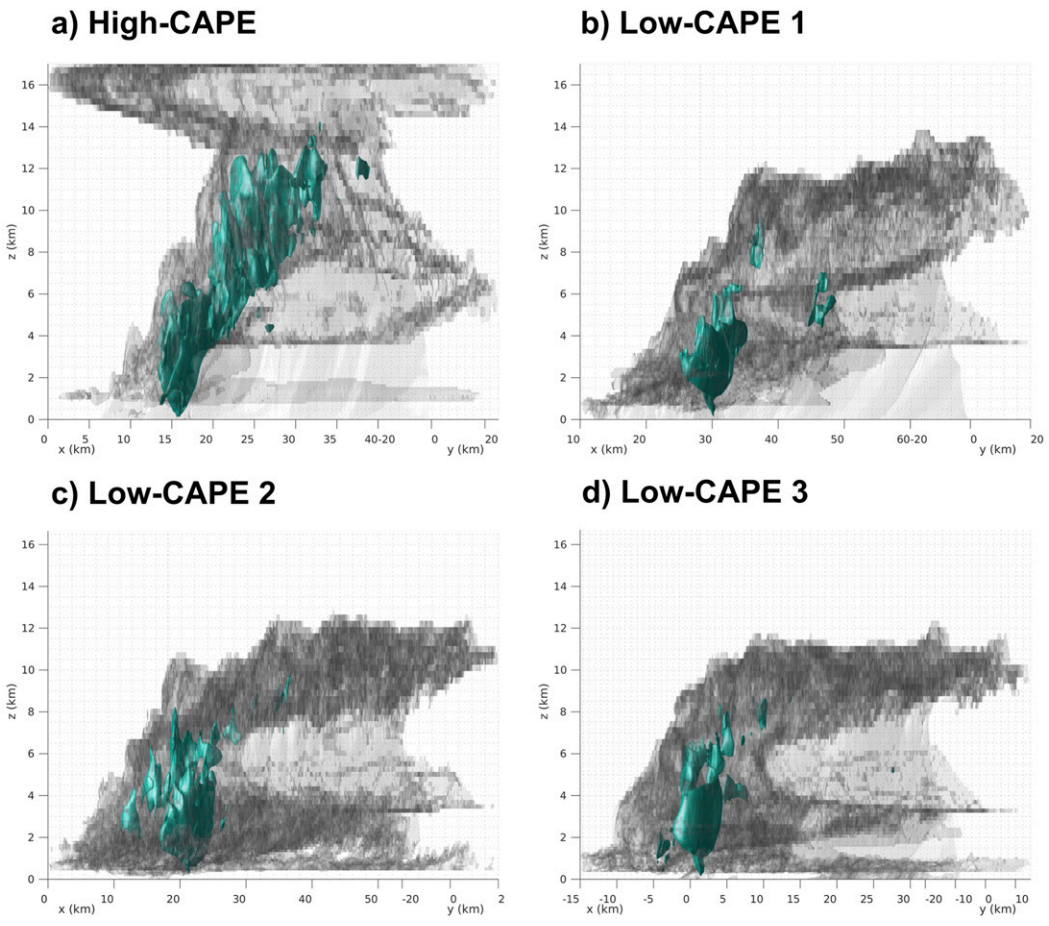

FIG. 9. Cloud and precipitation outlines (gray) and 15 m s^{-1} vertical velocity (teal) isosurfaces.

4. Results

a. Overview of simulations

All four simulations produce storms easily recognized as supercells by comparison to the archetype of Lemon and Doswell (1979). These discrete cells persist well over an hour beyond the end of updraft nudging and all produce tornado-like vortices of varying intensity and longevity. Figures 7–10 show the horizontal low-level structure of these storms around the time of vortex production. All have classical reflectivity structures (Fig. 7), e.g., hook echoes and sharp forward-flank reflectivity gradients. Intense rotating updrafts are adjacent to rear- and forward-flank downdrafts (Fig. 8). The storms' similar horizontal extent (each panel in Figs. 7 and 8 is 20 km × 20 km) suggests that these are not ''mini-supercells'' in the traditional sense. Three-dimensional structure, however, varies more noticeably with CAPE (Fig. 9). The high-CAPE supercell's visualized cloud and precipitation fields have a classic appearance (Fig. 9a). Its main updraft is a deep continuous column extending almost to its well-defined anvil near the EL. In contrast, the broadest regions of intense updraft in the low-CAPE storms are confined to the lowest few kilometers (Figs. 9b–d). Above this, individual midlevel to upper-level convective plumes or pulses appear detached from the mesocyclone below in a structure similar to the ''moderate evolution'' of Foote and Frank (1983). The low-CAPE cloud tops are also lower, consistent with lower ELs. HSLC storms' structure tends toward the high-precipitation end of the supercell spectrum (e.g., Figs. 7d and 9d) without the pronounced precipitation-free updraft base of the higher-CAPE storm (Fig. 9a). Also, though heavy precipitation is present in all four storms, time-averaged cold pools are consistently weaker in the low-CAPE cases (Fig. 10).

Time–height plots of these storms' maximum vertical velocity (w) capture the evolution of vertical structure over periods of interest (Fig. 11). Horizontal maximum values at each model level are calculated within a 20-km square centered on the 0.5–3 km AGL integrated updraft maximum. The high-CAPE storm has a deep intense updraft with many of its largest local maxima in the upper half of the troposphere. In contrast, the three low-CAPE storms' updrafts are weaker overall and have quasi-steady maxima between 2 and 4 km AGL, despite some deeper transient maxima that represent individual convective plumes. This resembles the HSLC updraft structure found by Murphy and Knupp (2013). Though the EL for all three low-CAPE base states is above 9 km, substantial w reaches that altitude only intermittently. The level of maximum detrainment [LMD; Mullendore et al. (2009)], typically

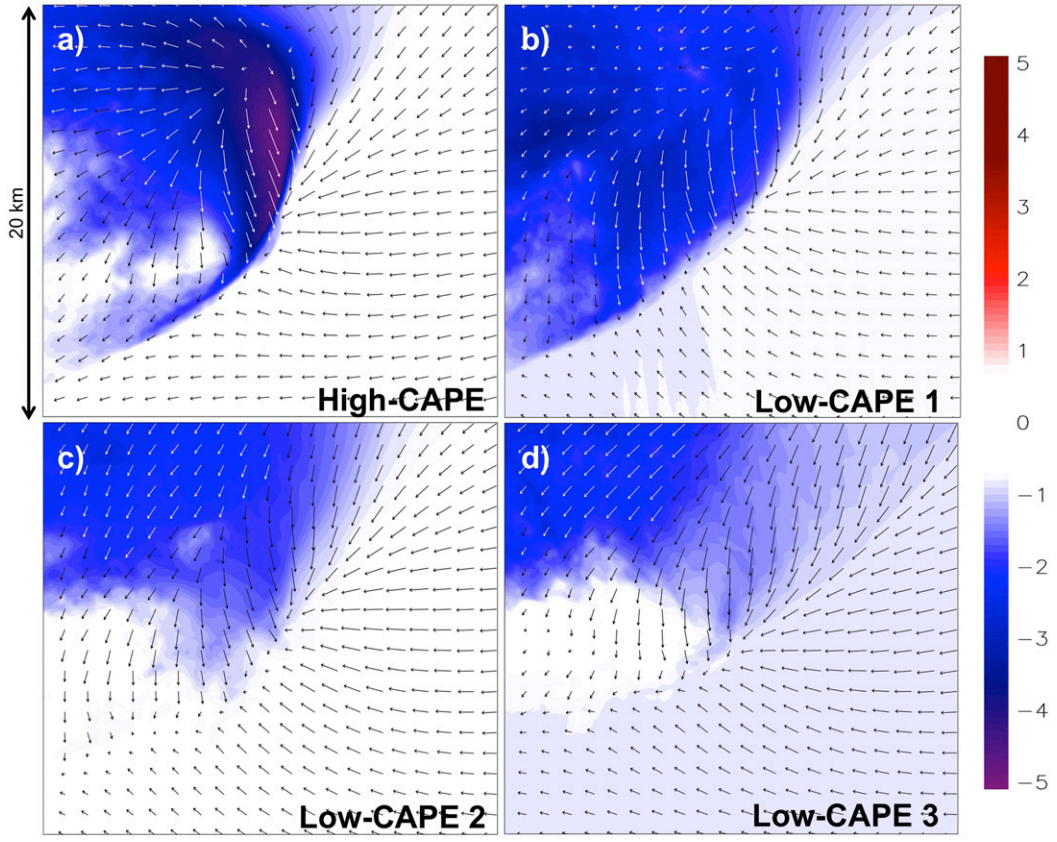

FIG. 10. Storm-centered time-averaged potential temperature perturbations (K) and wind at 10 m AGL for all four simulations, averaged over 20 min before and during vortex formation.

identified as a maximum in horizontal mass divergence in upper levels, offers a measure of storms' upper extent that may be more meaningful than cloud-top height alone. Mullendore (2019) demonstrated that supercells' LMDs commonly exceed the EL, while nonsupercell thunderstorms' LMDs are almost always below the EL. Figure 12 shows horizontally averaged horizontal mass divergence with downdrafts masked out, calculated similarly to the time–height profiles above but over a 30-km square region centered on the low-level updraft. The high-CAPE case has a pronounced LMD near but just below the EL. In contrast, the low-CAPE cases have LMDs ranging from one to several kilometers below the EL, and tend to have more vertically diffuse layers of mass divergence. Two likely reasons for the detrainment of most HSLC updrafts' mass disproportionately far below the EL—dynamic accelerations and dilution by entrainment—are explored in the next section.

Time–height plots of maximum vertical vorticity (ζ), created by the same method as the w time–height plots, highlight tornado-like vortices as vertically coherent maxima lasting at least a few minutes (Fig. 13). The vortices to be discussed in later sections occur from ~80 min onward in the high-CAPE storm and between 100 and 110 min in the three low-CAPE storms. Not surprisingly, the high-CAPE vortex is deeper and longer lived than the low-CAPE vortices. The decrease in the high-CAPE storm's maximum ζ late in the period is not dissipation of the tornado-like vortex, but a poorly resolved representation of vortex breakdown that persists for some time after the largest ζ is recorded. Figure 13 shows that these are not the only near-ground ζ maxima apparent in the low-CAPE storms. However, we focus on these particular vortices because of their subjective likeness to real mesocyclonic tornadoes (i.e., embedded within the mesocyclone instead of farther south along the gust front like a gustnado), their similar timing in each simulation, and their later occurrence than other features (i.e., farther removed from effects of artificial updraft nudging).

In this article we focus on the unique vertical accelerations that distinguish between the properties of the high- and low-CAPE supercells. Results below are divided into two sections in which parcel groups are analyzed with emphasis on their vertical accelerations: parcels that exceed certain w thresholds at a single time in each storm, and parcels that enter each tornado-like vortex near the ground. In a subsequent article, we will address the origins of vorticity and processes linked to tornadogenesis in these storms.

b. *Parcels with large vertical velocities*

Time series for groups of parcels that, at a single subjectively chosen "peak time" targeting a strong updraft in each run, all exceed 30 m s^{-1} upward velocity (50 m s^{-1} for the high-CAPE case) are shown in Fig. 14. In environments with reduced

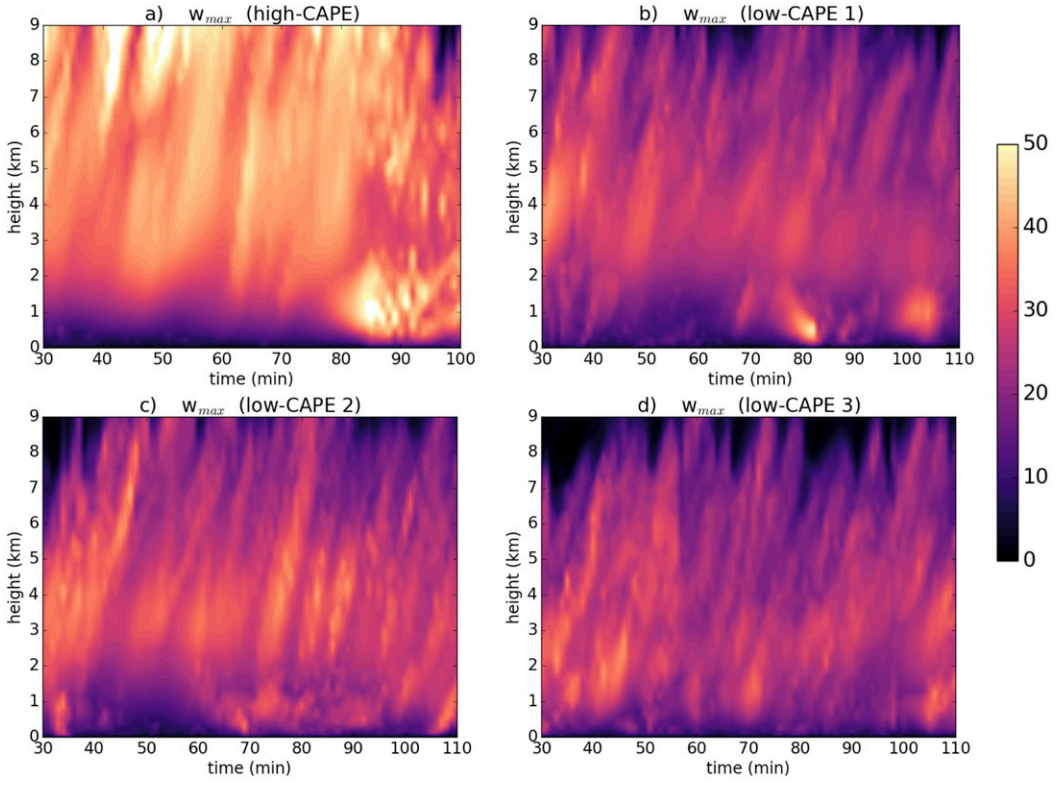

FIG. 11. Time–height maximum upward velocity ($\mathrm{m\,s^{-1}}$) in each simulated storm.

CAPE, parcel buoyancy can be expected to contribute less to updraft speeds, as in McCaul and Weisman (1996) and Murphy and Knupp (2013). This section quantifies that reduction and its relationship to updraft depth and speed. Making the Boussinesq approximation and neglecting Coriolis and friction, only two terms remain in the vertical momentum equation:

$$\frac{Dw}{Dt} = -\alpha_0 \frac{\partial p'}{\partial z} + B, \tag{1}$$

where the first term on the right-hand side is the VPPGA and the second is buoyancy, including hydrometeor loading. VPPGA may be separated into buoyant, linear dynamic, and nonlinear dynamic parts:

$$\frac{Dw}{Dt} = \underbrace{B - \alpha_0 \frac{\partial p'_B}{\partial z}}_{\text{ACCB}} \underbrace{- \alpha_0 \frac{\partial p'_{D_{\text{linear}}}}{\partial z} - \alpha_0 \frac{\partial p'_{D_{\text{nonlinear}}}}{\partial z}}_{\text{ACCD}}. \tag{2}$$

Forms of these terms are discussed in detail in, e.g., Rotunno and Klemp (1982, 1985) and Markowski and Richardson (2010). For the purposes of this paper, we often combine the buoyancy and buoyant VPPGA into a total buoyant acceleration (ACCB), and the two dynamic VPPGA terms into a total dynamic acceleration (ACCD). While the linear dynamic VPPGA is associated with an updraft in vertical shear and affects supercell motion, the nonlinear dynamic VPPGA (ACCDNL) is associated with updraft rotation (Weisman and Rotunno 2000) and dominates ACCD in the regions of most interest in this study. This echoes the primary role of ACCDNL in HSLC vortex production in the simulations of Sherburn and Parker (2019).

The p' terms are isolated using the iterative solver described by Coffer and Parker (2015). We decompose the entire storm's pressure field in this way every 10 s during key time periods. The near-perfect match between the CM1-computed VPPGA and the retrieved ACCD when buoyant effects are small (Fig. 14, third row) supports the retrievals' credibility. Mean parcel ACCD and ACCB are then integrated over the periods of interest to estimate the contribution of each, w_D and w_B, respectively, where the total $w = w_D + w_B$. Because the ACCD field is much noisier than ACCB in the relevant parts of the storms, these budgets make the most sense when ACCB is integrated (producing w_B) and the residual is treated as the dynamic contribution.

1) HIGH-CAPE UPDRAFT PARCELS

High-CAPE large-w parcels (Fig. 14) originate a few hundred meters AGL in the inflow region. They acquire mesocyclonic ζ ($\sim$0.01 $\mathrm{s^{-1}}$) below 1 km AGL and keep it throughout the depth of the storm. They steadily accelerate upward through midlevels and reach maximum velocity 10–11 km AGL (Figs. 14a,b). These parcels are clustered extremely tightly as they traverse the updraft; they were selected only by their instantaneous w, but all originate at the same level 6–7 min prior and ascend through the updraft at almost exactly

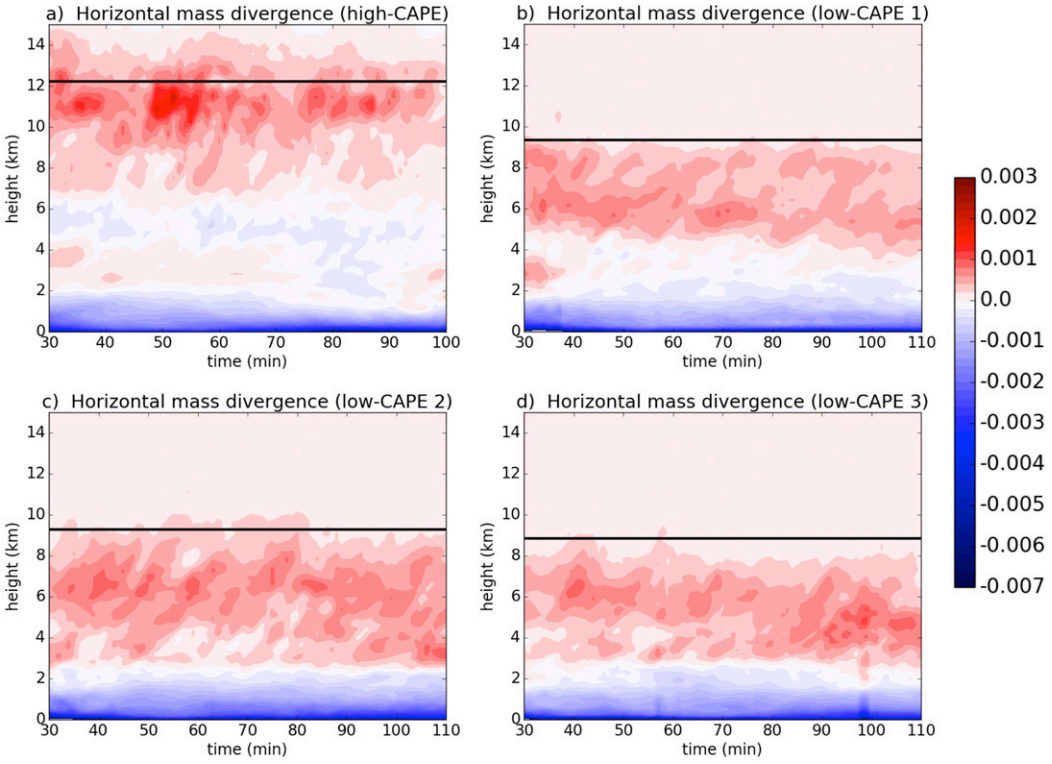

FIG. 12. Time–height total horizontal mass divergence ($kg\,s^{-1}$) in a 30-km square region centered on each simulated storm with downdrafts masked out. Black lines represent each environment's nominal equilibrium level.

the same rate. Conventional wisdom holds that ACCD substantially contributes to supercells' greatest updraft speeds [e.g., Weisman and Klemp (1984), Weisman and Rotunno (2000), and the "dynamic hypothesis" that Peters et al. (2019) found to be secondary to thermodynamics]. In the lower half of the troposphere, ACCD does dominate the high-CAPE updraft (Figs. 14a,c) and w_B is a small fraction of total w (Fig. 15). However, as parcels ascend above the midlevel mesocyclone, ACCD becomes negative and ACCB becomes large and positive (Figs. 14a,c). By the time these parcels reach $w = 50\,m\,s^{-1}$, about 70% of their w is attributable to ACCB (Fig. 15).

2) LOW-CAPE UPDRAFT PARCELS

Low-CAPE parcels with the largest upward velocities ($>30\,m\,s^{-1}$), though also originating in the lowest few hundred meters, behave much differently from their high-CAPE counterparts. The three low-CAPE simulations yield varying spatial distributions of large w at the times chosen for analysis. At times when simulated low-CAPE supercells are producing tornado-like vortices, those vortices and their immediate surroundings often contain the largest w in the entire storm. The group of large-w parcels in low-CAPE storm 1 (Figs. 14e–h) exemplifies this pattern. At this stage in the storm's life, the only parcels with $w > 30\,m\,s^{-1}$ are found around 1 km AGL and have fairly large ζ, 0.05–0.15 s^{-1}, near or within the tornado-like vortex. Their brief spike in w comes purely from upward ACCD associated with the vortex and low-level mesocyclone. Integrating ACCB (Fig. 15) confirms that buoyancy is responsible for none of the maximum w. Immediately afterward, these parcels experience downward ACCDNL above the vortex and low-level mesocyclone. With negligible ACCB, the mean w quickly returns to $0\,m\,s^{-1}$ and is even briefly negative just above 2 km AGL (Figs. 14e–g). This occurs only ~2 min after all parcels' w exceeds $30\,m\,s^{-1}$ upward.

Low-CAPE storm 2 (Figs. 14i–l) presents a different scenario. These large-w parcels are not part of a near-surface vortex but accelerate upward into a deeper updraft, acquiring w of $30\,m\,s^{-1}$ around 3 km AGL. Many parcels in this group maintain mesocyclonic ζ through midlevels, but at least some actually have negative ζ throughout their time in the updraft. The mean parcel becomes positively buoyant ~3 min before reaching maximum w. However, $B > 0$ is offset by the buoyant VPPGA in this region and ACCB remains negligible; ACCD dominates through the time of maximum w. Again, integration (Fig. 15) shows that ACCB contributes nothing to these parcels' maximum w—even though that maximum occurs more than 2 km above the theoretical LFC. Only around 5 km AGL, when downward ACCD has forced parcels to stop rising on average, does ACCB become appreciably positive (Figs. 14i–k).

Finally, the group of parcels with large w at the selected time in low-CAPE storm 3 (Figs. 14m–p) has some characteristics of both preceding groups. Most have ζ of 0.05–0.1 s^{-1} and reach their maximum w at an altitude of ~1 km from strong ACCD forcing, but on average they maintain w of $20\,m\,s^{-1}$ up to 4 km AGL. Like the updraft parcels in low-CAPE storm 2, they level off and lose all of their upward velocity due to downward

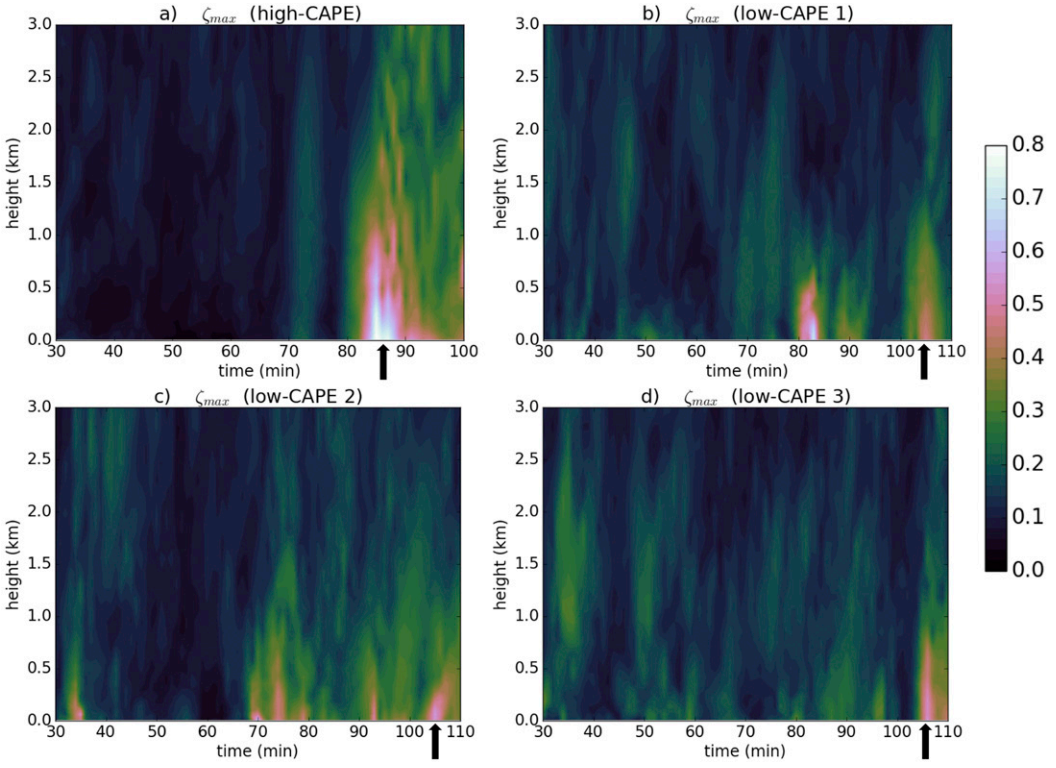

FIG. 13. Time–height maximum vertical vorticity (s^{-1}) in each simulated storm. Black arrows indicate the tornado-like vortices further investigated in each simulation.

ACCD as the total ACCB remains negligible (despite $B > 0$). As in the other two low-CAPE storms, mean parcel ascent vanishes far below the EL, corroborating the HSLC supercells' unexpectedly low LMDs in section 4a.

In summary, all four storms' large-w parcels at these times experience a spike in w to $\sim$30 m s^{-1} in low levels shortly after being ingested. In all four storms, this initial large w is entirely due to upward ACCD. The consistent dominance of dynamic lifting makes sense at a level where buoyancy is small, and where large mesocyclonic ζ and associated $p'_D < 0$ reside above. Subsequently, parcels encounter downward ACCD above the local p'_D minimum. High-CAPE parcels have sufficient ACCB to overcome this downward ACCD, continue upward toward their EL, and ultimately attain much larger w in the upper troposphere. Low-CAPE parcels do not; interestingly, all three groups of low-CAPE updraft parcels (with their varying degrees of influence from tornado-like vortices) encounter larger downward ACCD than the high-CAPE group. Parcel theory's prediction that thunderstorm updrafts monotonically increase in speed to some altitude near the EL is nowhere near valid in these HSLC cases. The three-dimensional differences in the ACCB and ACCD fields causing this behavior are shown in section 4d.

3) UPDRAFT ENTRAINMENT

Beyond their low-CAPE environments, another factor in HSLC storms' lack of ACCB is entrainment of dry midlevel air into updrafts, since less buoyant parcels require less evaporative cooling to completely remove their buoyancy. Figure 16 shows vertical profiles of the large-w parcels' buoyancy compared to a theoretical undiluted mixed-layer parcel. In all four storms, median updraft parcels match the theoretical parcels fairly well below 1.5–2 km AGL. Above that level, updrafts gradually lose buoyancy relative to the theoretical parcels, consistent with entrainment effects. The difference between the high- and low-CAPE storms is prominent above 4 km, where the high-CAPE updraft, due to its large theoretical parcel B, can withstand dilution from entrainment and still have enough B to continue accelerating upward. For the low-CAPE large-w parcels, the smaller theoretical parcel B means this dilution almost totally eliminates ACCB in the strongest updraft regions above the LFC.

Interestingly, there are some layers in all three low-CAPE updrafts where many parcels (in low-CAPE 2, even the median parcel) become *more* buoyant than the theoretical mixed-layer parcel. This mostly results from temporary downward excursions of positively buoyant updraft parcels. In Fig. 16, the gray lines representing individual parcels end where parcels attain their maximum altitude. So the numerous individual loops protruding to the right of the clustered traces indicate parcels that, despite being involved in the main updraft, briefly descend before ascending again to a higher altitude. There are large clusters of these loops 1–2 km AGL in low-CAPE 1, 3–6 km AGL in low-CAPE 2, and 3–6 km AGL in low-CAPE 3, with a few outliers also visible in other locations. The orientation of these loops relative to the buoyancy–height axes is

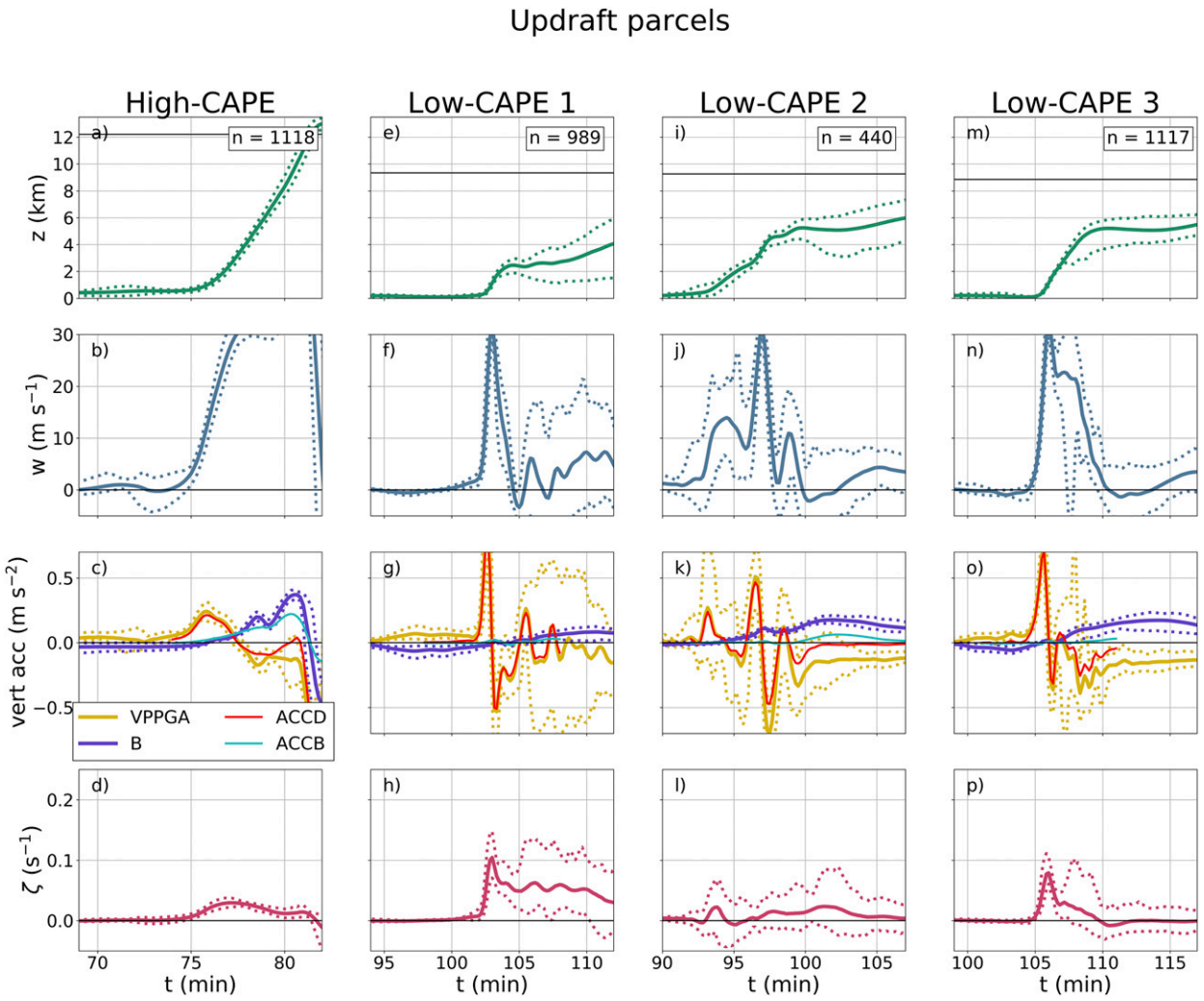

FIG. 14. Time series of (top to bottom) parcel altitude, vertical velocity, vertical acceleration terms, and vertical vorticity for parcels having large upward velocities at a single time in each simulated storm. Parcel group means are thick lines and the 10th and 90th percentiles are dashed. VPPGA and buoyancy are written out directly from CM1 at all output times. For the ACCB and ACCD series retrieved from p' decompositions by interpolating to parcel positions, only periods of most interest have been decomposed in this way and only means are shown.

consistent: B increases as parcels descend, and decreases as they ascend again. Presumably, these parcels encounter downward ACCD that overwhelms their modest ACCB, resulting in descent that is unsaturated over at least some of its depth. Given an ambient lapse rate less than dry neutral, as is the case at these levels in these environments, forced dry descent causes their B to increase. This could favor the downshear-tilted structure with multiple updraft plumes that is seen in Fig. 9, as many positively buoyant parcels struggle to ascend any farther as long as they are located above the lowest dynamic p' associated with the mesocyclone.

c. *Vortex parcels*

We now apply similar techniques to parcel groups that enter tornado-like vortices near the ground. These parcels' fates should help explain the vertical extent of those vortices. Are low-CAPE vortex trajectories just like high-CAPE vortex trajectories scaled somewhat shallower with their parent storms, or do parcels behave in a different pattern altogether? This section examines one tornado-like vortex in each storm occurring at least an hour after convective initiation to minimize effects of artificial forcing. Figures 17 and 18 display parcels that acquire $\zeta > 0.05\,\mathrm{s}^{-1}$ in the lowest 200 m AGL at a single output time as early as possible in each vortex's life.

1) HIGH-CAPE VORTEX PARCELS

While vortex parcels in all four storms arrive at their vortices from the low levels of the outflow sector north of the vortex location (Fig. 18) with negative or neutral buoyancy, those in the high-CAPE storm (Figs. 17a–d) are most negatively buoyant, consistent with its stronger near-surface cold pool (Fig. 10). Parcels entering the high-CAPE vortex experience

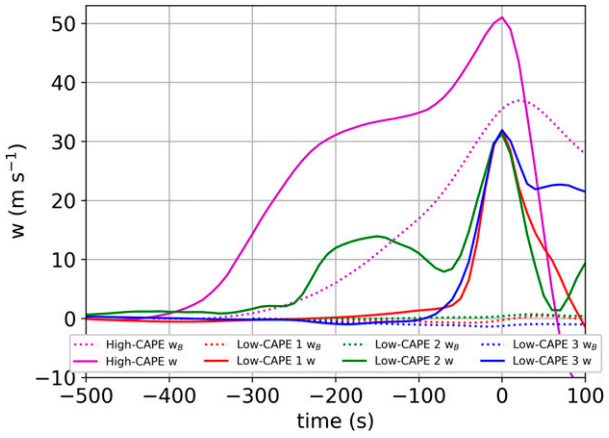

FIG. 15. Time series of the large-w parcel groups' mean vertical velocity (solid lines) and the w_B (dotted lines) produced by integrating ACCB for all four storms. Times are relative to time of maximum w.

sudden large upward ACCD (Fig. 17c) from the nonlinear term, much like updraft parcels entering the low-level mesocyclone. They reach a mean w of ~28 m s^{-1} near 1 km AGL (Figs. 17a,b) before encountering downward ACCD above the vortex and near-ground mesocyclone (Fig. 17c). Around the same time, ACCB becomes positive and offsets some of the downward ACCD (Fig. 17c). Integration shows that less than 5 min after ingestion, ACCB has imparted 10 m s^{-1} ascent to the high-CAPE vortex parcels (Fig. 19). Most continue upward in a deep, buoyant column, and many approach the EL (Fig. 18a). They retain their large ζ to altitudes of several km (Figs. 17a,d). These trajectories behave as might be expected from any number of existing higher-CAPE studies [e.g., the rapid monotonic ascent of tornadic parcels in Coffer and Parker (2017), or the coherent columnar vortex extending through most of the storm's depth simulated by Orf et al. (2017)].

2) LOW-CAPE VORTEX PARCELS

A wider range of vortex parcel behavior exists among the three low-CAPE storms analyzed here. A vortex of interest occurs at roughly the same time in each low-CAPE simulation, so we refer to these three vortices by the same numbers as their parent storms. Parcels in low-CAPE vortex 1 (Figs. 17e–h) exhibit the same initial ACCD-driven spike in w. They ascend rapidly to 1.5–2 km AGL, encounter downward ACCD above the vortex and low-level mesocyclone, and abruptly stop ascending. The mean w becomes negative only 2–3 min after vortex ingestion. Both of these sudden swings in w are driven entirely by ACCD; the integrated ACCB is negligible throughout this period. The onset of mean subsidence below 2 km AGL is a new and unexpected finding that contrasts sharply with high-CAPE behavior. It is also a plausible explanation for at least some HSLC vortices' shallowness, opposing vertical advection of large ζ into a deeper column. At the level of stagnation, many of the parcels also disperse horizontally away from the vortex top (Fig. 18b).

In low-CAPE vortex 2, this behavior is less extreme. These parcels (Figs. 17i–l)experience the same upward and downward ACCD associated with the vortex and low-level mesocyclone, resulting in a rapid spike and decline in w as in low-CAPE 1. However, the mean w does not become negative and most parcels slowly ascend above the vortex top into midlevels. Still, ACCB and its integrated contribution to w are negligible for at least 5 min following ingestion, including the time period where downward ACCD greatly slows parcel ascent.

Finally, parcel behavior in low-CAPE vortex 3 (Figs. 17m–p) falls somewhere between low-CAPE 1 and 2. As in all four

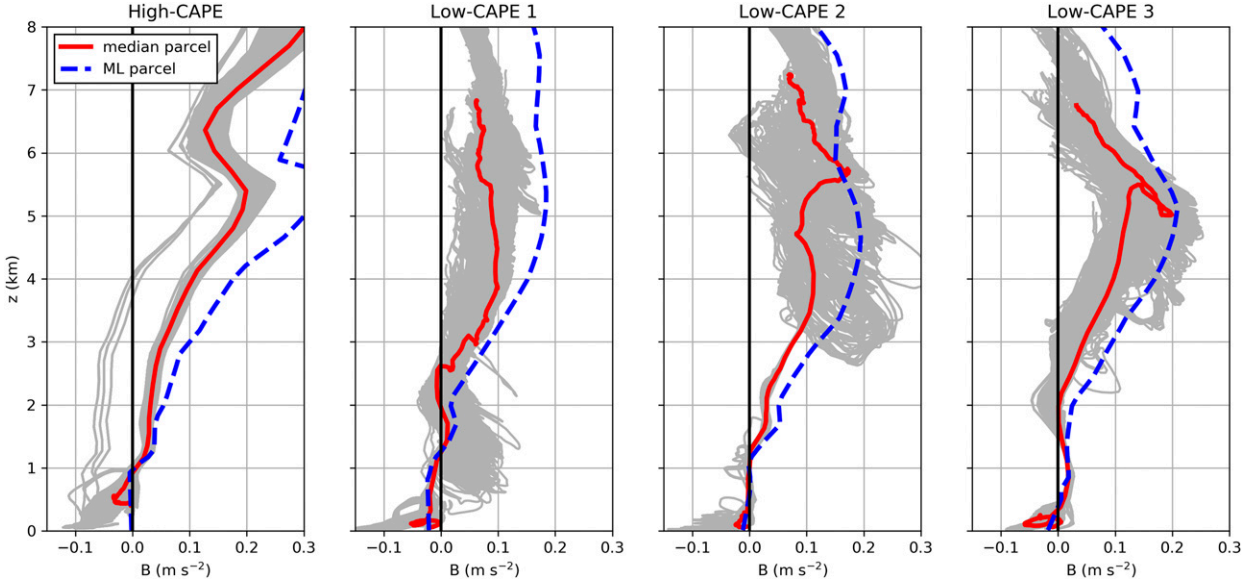

FIG. 16. Vertical profiles of buoyancy of large-w parcels in each storm (gray), their median (red), and a theoretical 100-hPa mixed-layer parcel in the simulation base state (blue dashed).

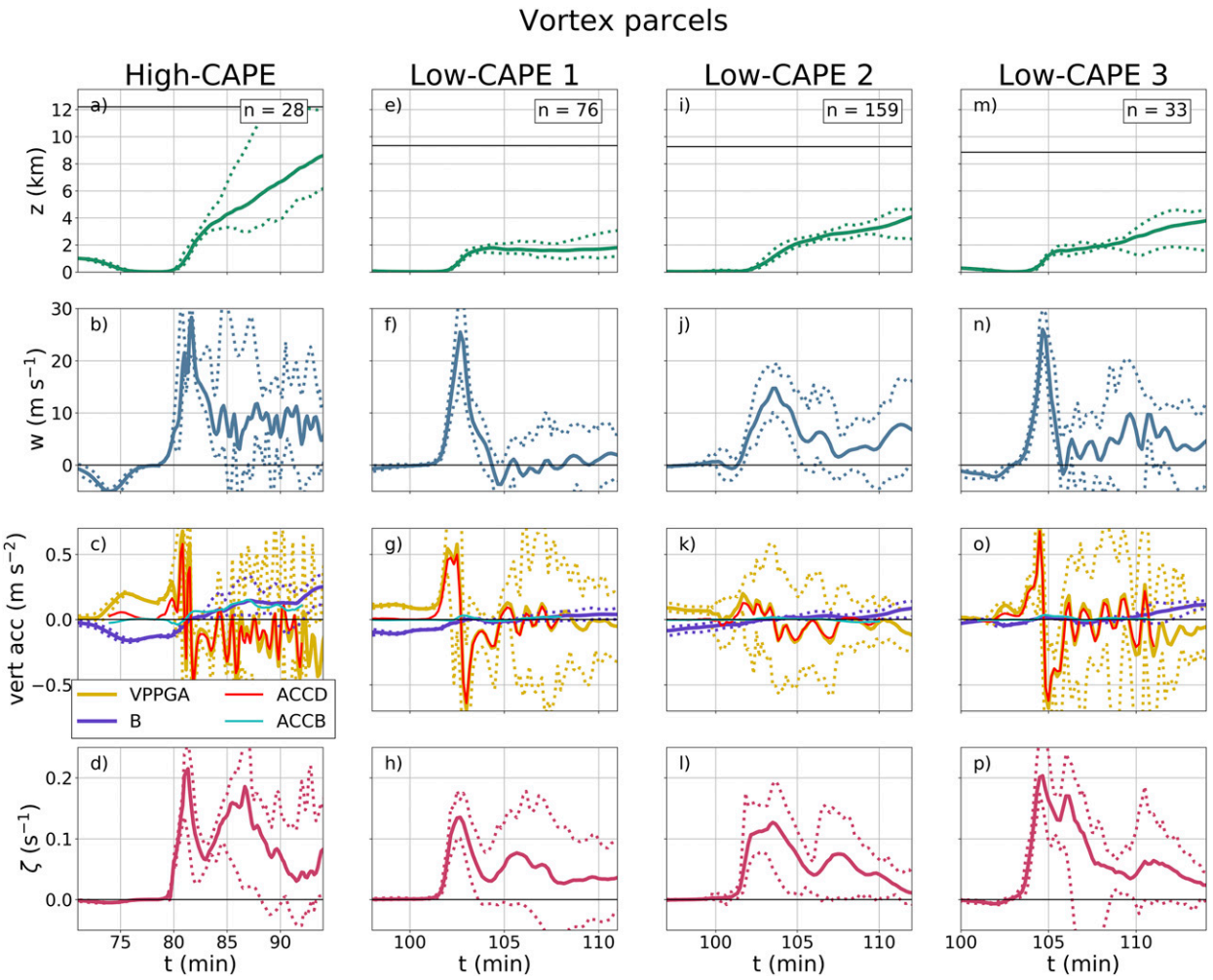

FIG. 17. As in Fig. 14, but for parcels entering each storm's tornado-like vortex near the ground at a single time.

storms, parcels are subject to sudden large upward ACCD while entering the vortex, followed within a minute by similarly large downward ACCD above it. Their mean w becomes negative above the vortex, repeating the unexpected sinking found in low-CAPE vortex 1, but they do not remain trapped at the vortex top as long. Integrated ACCB is again negligible in the key minutes after ingestion (Fig. 19d).

In general, none of the low-CAPE vortex parcels are able to transport large ζ as high, or as quickly, as their high-CAPE counterparts. The upward ACCB that allows high-CAPE parcels to maintain mean w around 8–10 m s^{-1} amid downward ACCD is absent at the same location near the top of low-CAPE vortices. This causes low-CAPE vortex parcels to stagnate, or at least rise much more slowly, near the vortex top. HSLC vortex parcels also disperse horizontally away from the vortex top while high-CAPE vortex parcels remain in a coherent column to higher altitudes. In this sense higher-CAPE vortices, at least early in life, are directly coupled to their parent updrafts in a way that HSLC vortices may not be. This broadening of HSLC vortices' associated circulation probably further complicates discrimination of radar signatures at long distances.

d. *Vertical acceleration fields around vortices*

To complement the updraft and vortex parcel trajectories, three-dimensional isosurfaces of the dominant vertical accelerations—ACCDNL and ACCB—are shown for all four cases (Figs. 20 and 21). These depict vortex-centered 5-min averages beginning 1 min before the parcel groups in the above subsection enter their respective vortices. [Total ACCD isosurfaces (not shown) are almost identical to these ACCDNL isosurfaces.] The structure of the ACCDNL and ACCB fields clarifies how buoyancy's role varies from high to low CAPE. In the lowest 2 km of all four storms, there is a clear dipole in ACCDNL associated with the vortex (black surface of ζ near the ground) and near-ground mesocyclone, with upward accelerations (yellow surface) below and downward accelerations (blue surface) above. In the high-CAPE storm and low-CAPE storms 1 and 3, a similar dipole is associated with the midlevel

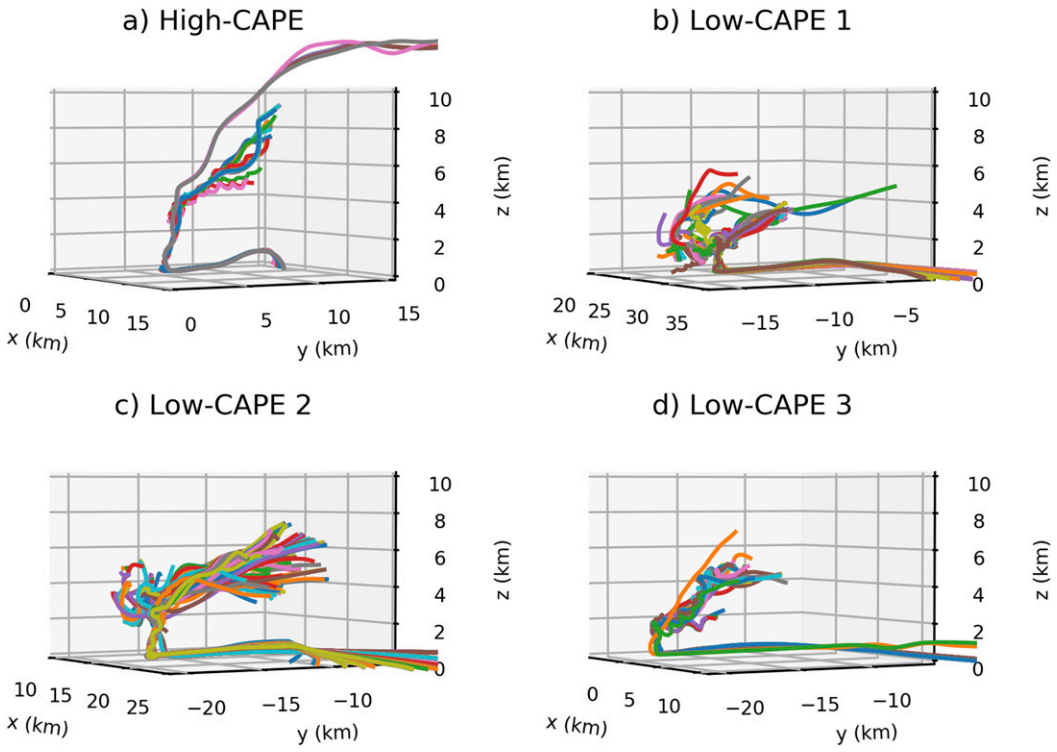

FIG. 18. Trajectories of the selected vortex parcel groups in each storm, ending 15 min after ingestion.

mesocyclone (3–6 km AGL in the high-CAPE storm, 2–5 km in the low-CAPE storms). The high-CAPE storm also displays a footlike extension of paired upward and downward ACCDNL associated with a corridor of large, initially horizontal streamwise vorticity emanating from the forward flank just above the ground and being tilted into the low-level mesocyclone. But the location and spatial extent of appreciable ACCB (magenta surface) is the key difference between high- and low-CAPE storms. The high-CAPE storm features a large column of ACCB $> 0.05\,\mathrm{m\,s^{-2}}$. This column intersects the top of the vortex and low-level mesocyclone and encloses the midlevel mesocyclone. In contrast, the same magnitude of ACCB is completely disconnected from the low-level features in the HSLC storms. The top-down views in Fig. 21 show that ACCB (magenta) is displaced downshear from the low-level mesocyclone (blue–yellow dipole), and often even downshear from the midlevel mesocyclone. This structure is consistent with HSLC vortex parcels' failure to become positively buoyant in the minutes after vortex entry when they encounter downward ACCDNL. It can also be applied to the HSLC updraft parcels that acquire large w in the mesocyclone, explaining why they only experience positive ACCB after leaving the region of stronger dynamic lifting.

5. Conclusions

Idealized simulations demonstrate differing kinematics and dynamics of supercells in realistic high- and low-CAPE environments. These simulations offer dynamical explanations for some observable characteristics of HSLC storms. The main findings are:

1) Simulated HSLC supercells' updraft maxima are primarily dynamically driven and occur at much lower altitudes than higher-CAPE storms' updraft maxima, which occur near the EL and are mostly buoyancy-driven. This agrees with previous simulations in tropical cyclone environments and HSLC pseudo-dual-Doppler analyses. Horizontal divergence profiles suggest little of the mass in HSLC storms' main updrafts approaches the nominal EL.

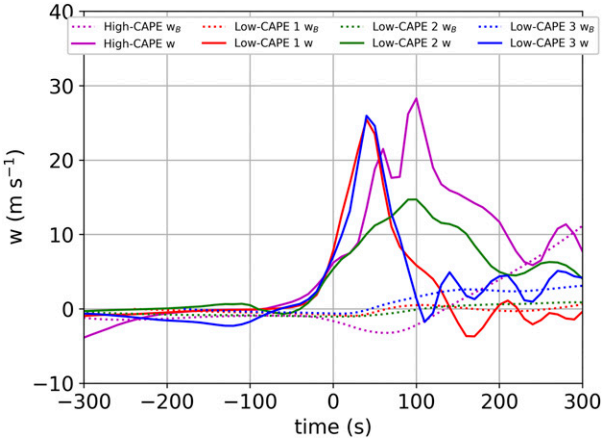

FIG. 19. As in Fig. 15, but for vortex parcel groups, and with times relative to vortex ingestion.

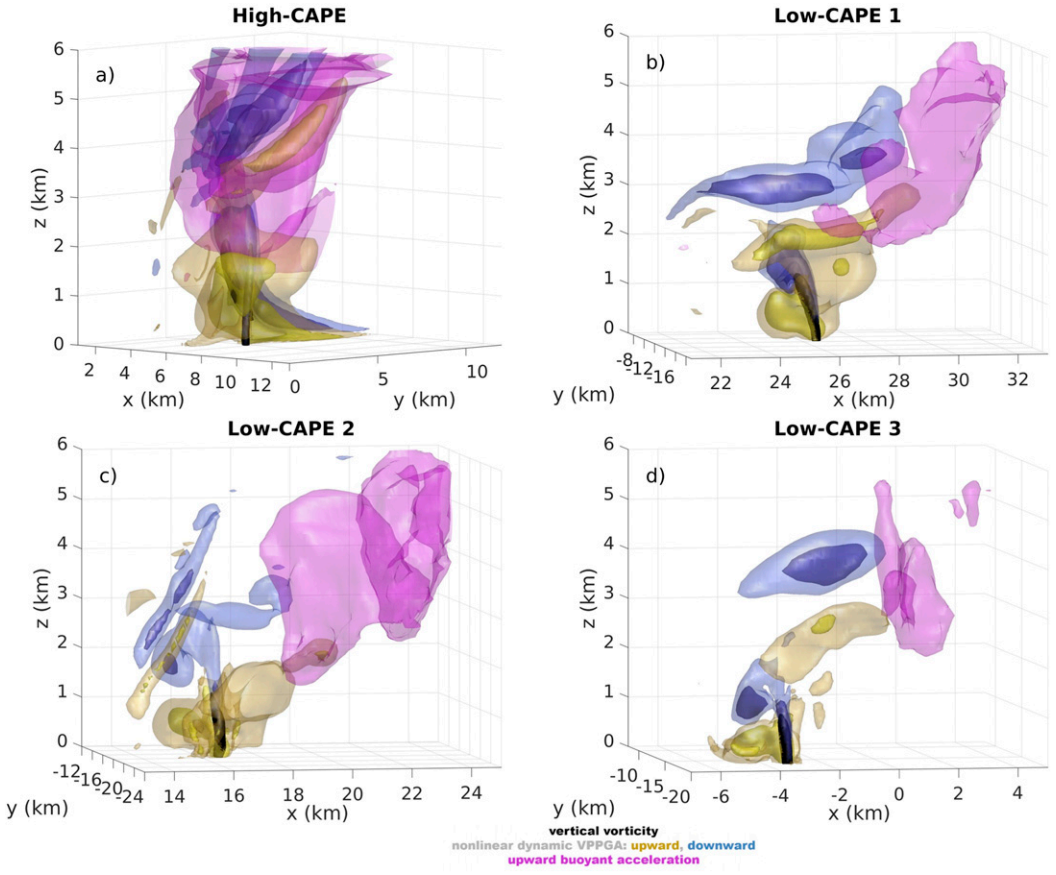

FIG. 20. Isosurfaces of 0.15 and 0.25 m s^{-2} ACCDNL (yellow upward, blue downward), 0.05 m s^{-2} upward ACCB (magenta), and 0.1 s^{-1} vertical vorticity (black). Fields are vortex-centered time averages over the first 5 min of each vortex's life cycle.

2) A major cause of HSLC vortices' shallowness is the inability of reduced buoyancy to overcome downward ACCD near the top of the low-level mesocyclone and carry high-ζ parcels into a deeper column. Stagnation of vortex parcels near the vortex top—even mean parcel subsidence in two of three cases—opposes vertical growth of vortices and appears to be a novel behavior among supercell simulations.

This second point in particular is operationally important in HSLC events. Vortex parcels' failure to rise through the downward ACCD near vortex top is probably related to the radar detection difficulties described by Davis and Parker (2014). This behavior appears more directly dependent on parcel buoyancy than on the parent storm's depth. This has two implications. First, radar operators should be aware that low-CAPE supercells may have elusively shallow vortex signatures even if neither the tropopause nor cloud tops are unusually low. Second, the importance of ACCB around vortex top may offer further physical justification for HSLC observational studies that emphasize CAPE or lapse rates in the 0–3-km layer (e.g., Guyer et al. 2006; Sherburn et al. 2016) for prediction of significant severe weather. Thermodynamic profiles permitting more ACCB in the lowest levels might be associated with vortex trajectories more like those in the deeper, longer-lasting, more intense high-CAPE vortex.

The importance of small-scale ACCD in governing the depth of these storms' key features, as well as the narrowness of real tornadoes in these marginally supportive environments, underscores the need to continue modeling HSLC storms at increasing resolution. Future work should include extension to different HSLC events' environments. While the 31 March 2016 case was selected because of the VORTEX-SE observations, its relatively well-mixed PBL and dry air aloft are not present in all HSLC events. A wide range of the higher-CAPE parameter space has been modeled at comparable resolution; this should be a goal for low CAPE as well. In particular, vortex parcel behavior in these cases suggests that future experiments should vary CAPE within shallow layers, like 0–3 km AGL. Regarding the modeling techniques themselves, work is needed to represent surface friction more effectively than the attempts documented in the appendix, and it might be worth investigating why model analyses serve as better base states than observed soundings in this horizontally homogeneous framework. On the observational side, true multi-Doppler analyses of HSLC supercells are highly desirable for validating these simulations. Finally, it is worth asking whether the

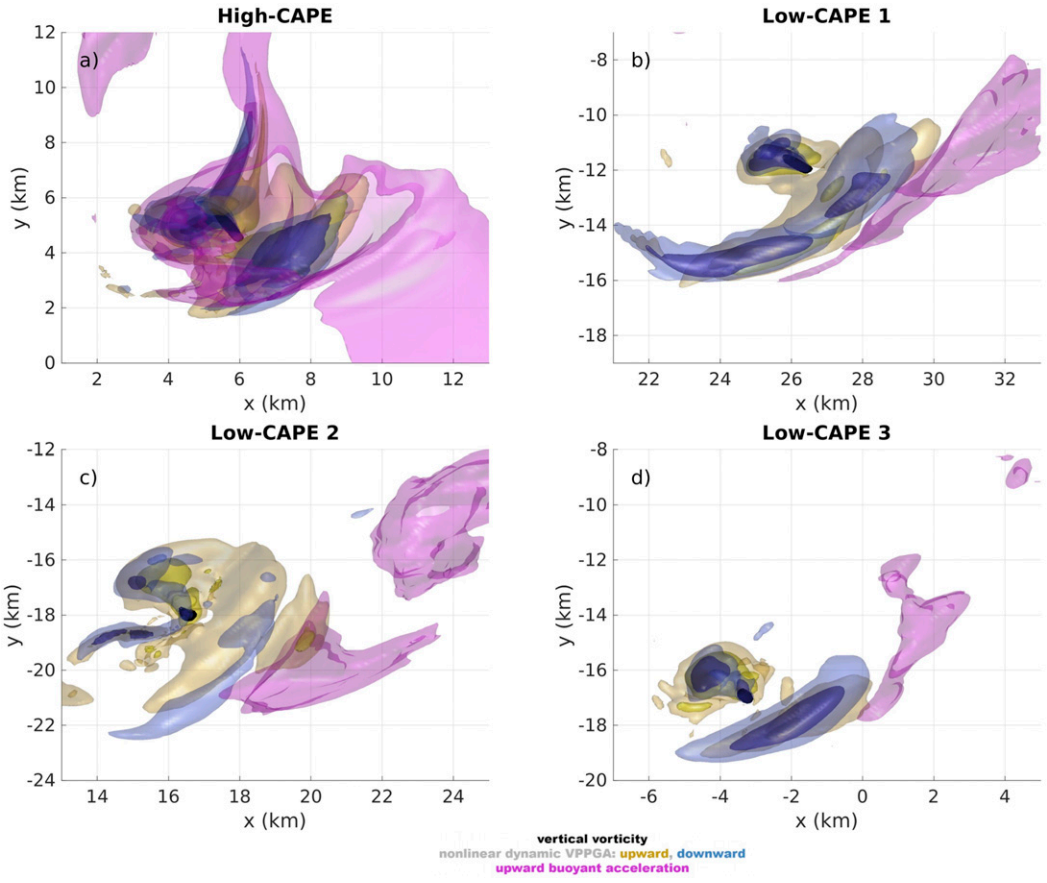

FIG. 21. As in Fig. 20, but viewed from the top down.

widely accepted dominance of baroclinically generated vorticity in supercell tornadogenesis generalizes to HSLC storms with weaker cold pools and often larger environmental vorticity. This question will be addressed in a subsequent article using these simulations.

Acknowledgments. The authors are grateful for input and support from the Convective Storms Group at NC State as well as Sandra Yuter, Gary Lackmann, and Johannes Dahl. We appreciate the contributions of three reviewers. All simulations shown were conducted on NCAR's Cheyenne. MetPy, Py-ART, and SHARPpy packages were used in some calculations and visualizations. This work was made possible by NOAA Grants NA15OAR4590235, NA16OAR4590213, and NA17NWS4680002.

Data availability statement. Model code, namelist settings, base-state profiles, and limited model output are available from the authors upon request.

APPENDIX

Sensitivities to Parameterizations

Though not the primary goal of this study, it is worthwhile to document large sensitivities to a couple of widely used model parameterizations. These sensitivities seem greater in HSLC parameter spaces than in higher-CAPE environments and are described here for the benefit of future HSLC modeling.

a. Microphysics

The weak cold pools in some of the HSLC cases are sensitive to the choice of microphysics. In particular, the Morrison et al. (2005) two-moment scheme produces abundant cold outflow not easily reconciled with surface observations from the 31 March 2016 event; Fig. A1 shows an example of this. As implemented in CM1, this scheme allows only one "large ice" category, which is set to hail or graupel. This creates a dilemma unique to HSLC simulations. Forcing all large ice to be hail instead of graupel—the default in CM1—produces large amounts of hail in low-CAPE updrafts with modest vertical velocities. This hail falls out before it can be carried downshear, concentrating latent cooling in the immediate forward-flank and rear-flank downdraft area. Choosing graupel and prohibiting hail yields a milder cold pool but results in abundant ice being advected far downstream in high-shear environments, creating an unrealistic streamer of light to moderate precipitation extending many km out of the forward flank. In short, there should probably be some hail in low-CAPE supercells, but not copious hail at the surface. A scheme with separate classes for graupel and hail is best equipped to handle

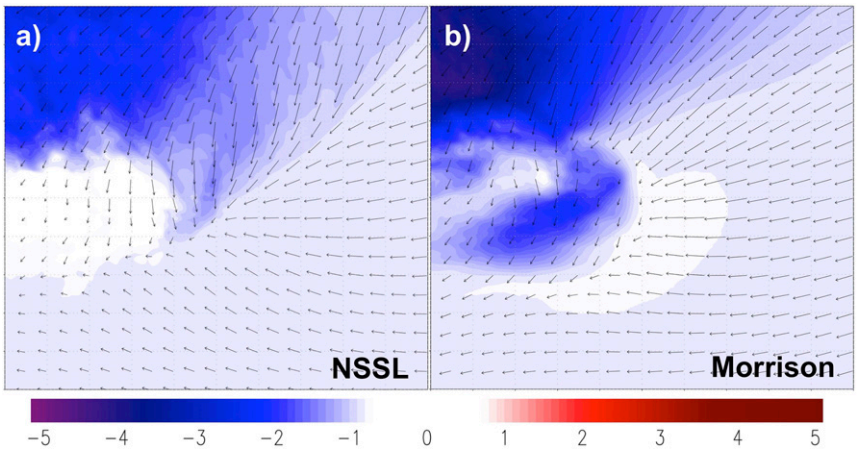

FIG. A1. Time-averaged potential temperature perturbations (K) and wind at 10 m AGL for low-CAPE 3, with (a) NSSL microphysics as in Fig. 10d and (b) Morrison microphysics and large ice set to hail.

this, which is one reason for choosing the NSSL two-moment scheme (Mansell et al. 2010).

b. Lower boundary condition

A series of modeling studies (Schenkman et al. 2014; Roberts et al. 2016; Roberts and Xue 2017) has attributed tornado vorticity (at least very early in simulated storms) to frictional generation. However, in our set of HSLC simulations, parameterization of friction with the semislip lower boundary condition strongly and systematically *inhibits* tornado-like vortex production (Fig. A2).

Specifically, the large horizontal accelerations and accompanying vorticity stretching immediately behind the gust front

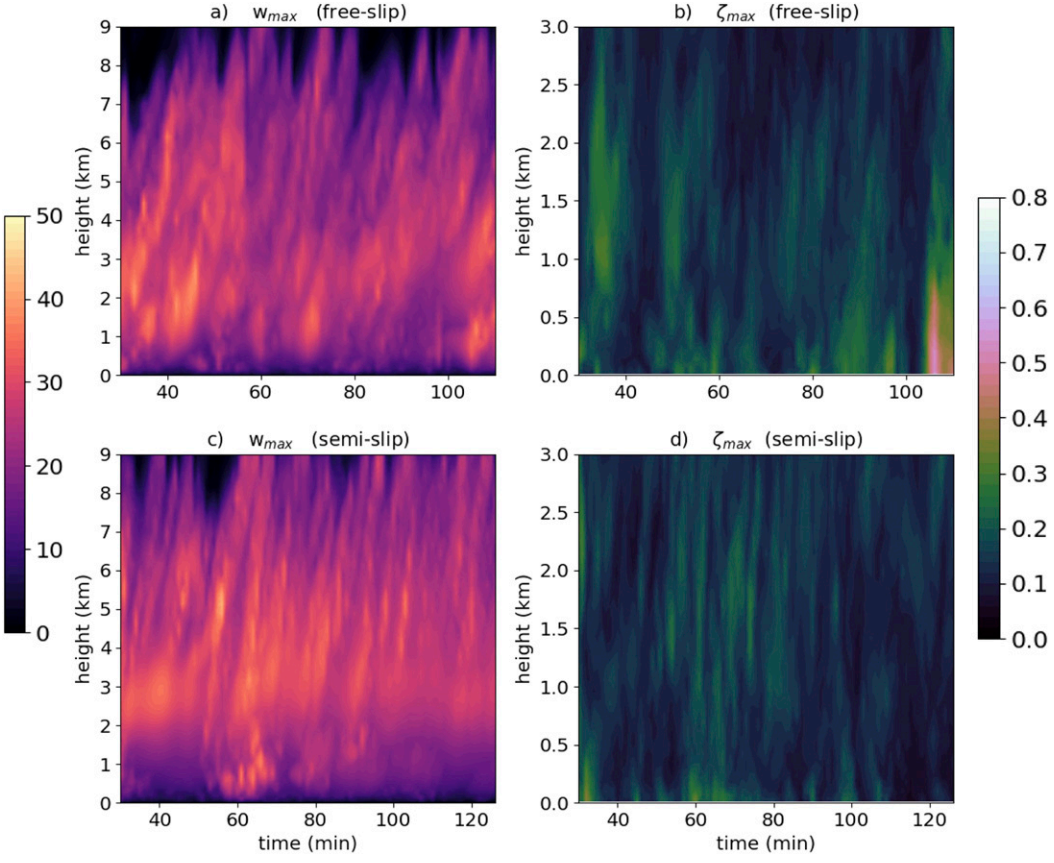

FIG. A2. (a) Maximum vertical velocity ($m\,s^{-1}$) and (b) maximum vertical vorticity (s^{-1}) from Figs. 11a and 13a. (c),(d) As in (a) and (b), respectively, but rerun with the semislip lower boundary condition.

are severely damped by the semislip condition. Wind profiles outside the storm are minimally affected. The amount of drag does not seem to matter; the effect is comparable even using the roughness of a water surface (not shown). Sherburn (2018) documented a similar effect with low CAPE. Yet this does not prove that the free-slip simulations are seriously flawed in their representation of vortexgenesis; Markowski et al. (2019) noted that outflow wind profiles from VORTEX-SE deviate widely from the predictions of Monin–Obukhov theory (Monin and Obukhov 1954), and concluded that the related semislip parameterization does not necessarily add realism to storm simulations. Furthermore, Markowski and Bryan (2016) described unrealistically large vertical wind shear near the ground produced by insufficiently turbulent large-eddy simulations combined with a lower boundary condition other than free-slip. More work is still needed to clarify the real impacts of friction in both high- and low-CAPE storms.

REFERENCES

Anderson-Frey, A., Y. P. Richardson, A. R. Dean, R. L. Thompson, and B. T. Smith, 2016: Investigation of near-storm environments for tornado events and warnings. *Wea. Forecasting*, **31**, 1771–1790, https://doi.org/10.1175/WAF-D-16-0046.1.

——, ——, ——, ——, and ——, 2018: Tornadic near-storm environments of the southeastern United States. *29th Conf. on Severe Local Storms*, Stowe, VT, Amer. Meteor. Soc., 1.1, https://ams.confex.com/ams/29SLS/webprogram/Paper348273.html.

Ashley, W., 2007: Spatial and temporal analysis of tornado fatalities in the United States: 1880–2005. *Wea. Forecasting*, **22**, 1214–1228, https://doi.org/10.1175/2007WAF2007004.1.

Betts, A., 1984: Boundary layer thermodynamics of a High Plains severe storm. *Mon. Wea. Rev.*, **112**, 2199–2211, https://doi.org/10.1175/1520-0493(1984)112<2199:BLTOAH>2.0.CO;2.

Browning, K., 1964: Airflow and precipitation trajectories within severe local storms which travel to the right of the winds. *J. Atmos. Sci.*, **21**, 634–639, https://doi.org/10.1175/1520-0469(1964)021<0634:AAPTWS>2.0.CO;2.

Bryan, G. H., and J. M. Fritsch, 2002: A benchmark simulation for moist nonhydrostatic numerical models. *Mon. Wea. Rev.*, **130**, 2917–2928, https://doi.org/10.1175/1520-0493(2002)130<2917:ABSFMN>2.0.CO;2.

Coffer, B. E., and M. D. Parker, 2015: Impacts of increasing low-level shear on supercells during the early evening transition. *Mon. Wea. Rev.*, **143**, 1945–1969, https://doi.org/10.1175/MWR-D-14-00328.1.

——, and ——, 2017: Simulated supercells in nontornadic and tornadic VORTEX2 environments. *Mon. Wea. Rev.*, **145**, 149–180, https://doi.org/10.1175/MWR-D-16-0226.1.

Cohen, A. E., 2010: Indices of violent tornado environments. *Electron. J. Oper. Meteor.*, **11** (6), http://nwafiles.nwas.org/ej/pdf/2010-EJ6.pdf.

——, S. M. Cavallo, M. C. Coniglio, and H. E. Brooks, 2015: A review of planetary boundary layer parameterization schemes and their sensitivity in simulating southeastern U.S. cold season severe weather environments. *Wea. Forecasting*, **30**, 591–612, https://doi.org/10.1175/WAF-D-14-00105.1.

——, ——, ——, ——, and I. L. Jirak, 2017: Evaluation of multiple planetary boundary layer parameterization schemes in southeast U.S. cold season severe thunderstorm environments. *Wea. Forecasting*, **32**, 1857–1884, https://doi.org/10.1175/WAF-D-16-0193.1.

Dahl, J. M. L., M. D. Parker, and L. J. Wicker, 2014: Imported and storm-generated near-ground vertical vorticity in a simulated supercell. *J. Atmos. Sci.*, **71**, 3027–3051, https://doi.org/10.1175/JAS-D-13-0123.1.

Davies, J. M., 2006: Tornadoes with cold core 500-mb lows. *Wea. Forecasting*, **21**, 1051–1062, https://doi.org/10.1175/WAF967.1.

Davis, J. M., and M. D. Parker, 2014: Radar climatology of tornadic and nontornadic vortices in high-shear, low-CAPE environments in the mid-Atlantic and southeastern United States. *Wea. Forecasting*, **29**, 828–853, https://doi.org/10.1175/WAF-D-13-00127.1.

Dean, A. R., and R. S. Schneider, 2008: Forecast challenges at the NWS Storm Prediction Center relating to the frequency of favorable severe storm environments. *24th Conf. on Severe Local Storms*, Savannah, GA, Amer. Meteor. Soc., 9A.2, http://ams.confex.com/ams/24SLS/techprogram/paper_141743.htm.

Foote, G. B., and H. W. Frank, 1983: Case study of a hailstorm in Colorado. Part III: Airflow from triple-Doppler measurements. *J. Atmos. Sci.*, **40**, 686–707, https://doi.org/10.1175/1520-0469(1983)040<0686:CSOAHI>2.0.CO;2.

Guyer, J. L., A. K. Kis, K. N. Venable, and D. A. Imy, 2006: Cool season significant (F2–F5) tornadoes in the Gulf Coast states. *23rd Conf. on Severe Local Storms*, St. Louis, MO, Amer. Meteor. Soc., 4.2, http://ams.confex.com/ams/23SLS/techprogram/paper_115320.htm.

Hoxit, L. R., and C. F. Chappell, 1975: Tornado outbreak of 3–4 April 1974: Synoptic analysis. NOAA Tech Rep. ERL 388-APCL 37, 48 pp.

Kennedy, P. C., N. E. Westcott, and R. W. Scott, 1993: Single-Doppler radar observations of a mini-supercell tornadic thunderstorm. *Mon. Wea. Rev.*, **121**, 1860–1870, https://doi.org/10.1175/1520-0493(1993)121<1860:SDROOA>2.0.CO;2.

King, J. R., M. D. Parker, K. D. Sherburn, and G. M. Lackmann, 2017: Rapid evolution of cool season, low-CAPE severe thunderstorm environments. *Wea. Forecasting*, **32**, 763–779, https://doi.org/10.1175/WAF-D-16-0141.1.

Klemp, J. B., and R. B. Wilhelmson, 1978: The simulation of three-dimensional convective storm dynamics. *J. Atmos. Sci.*, **35**, 1070–1096, https://doi.org/10.1175/1520-0469(1978)035<1070:TSOTDC>2.0.CO;2.

Lemon, L. R., and C. A. Doswell, 1979: Severe thunderstorm evolution and mesocyclone structure as related to tornadogenesis. *Mon. Wea. Rev.*, **107**, 1184–1197, https://doi.org/10.1175/1520-0493(1979)107<1184:STEAMS>2.0.CO;2.

Mansell, E. R., C. L. Ziegler, and E. C. Bruning, 2010: Simulated electrification of a small thunderstorm with two-moment bulk microphysics. *J. Atmos. Sci.*, **67**, 171–194, https://doi.org/10.1175/2009JAS2965.1.

Markowski, P. M., and J. M. Straka, 2000: Some observations of rotating updrafts in a low-buoyancy, highly sheared environment. *Mon. Wea. Rev.*, **128**, 449–461, https://doi.org/10.1175/1520-0493(2000)128<0449:SOORUI>2.0.CO;2.

——, and Y. Richardson, 2010: *Mesoscale Meteorology in Midlatitudes*. Wiley-Blackwell, 407 pp.

——, and G. H. Bryan, 2016: LES of laminar flow in the PBL: A potential problem for convective storm simulations. *Mon. Wea. Rev.*, **144**, 1841–1850, https://doi.org/10.1175/MWR-D-15-0439.1.

——, N. T. Lis, D. D. Turner, T. R. Lee, and M. S. Buban, 2019: Observations of near-surface vertical wind profiles and vertical momentum fluxes from VORTEX-SE 2017: Comparisons to Monin–Obukhov similarity theory. *Mon. Wea. Rev.*, **147**, 3811–3824, https://doi.org/10.1175/MWR-D-19-0091.1.

McCaul, E. W., 1991: Buoyancy and shear characteristics of hurricane tornado environments. *Mon. Wea. Rev.*, **119**, 1954–1978, https://doi.org/10.1175/1520-0493(1991)119<1954:BASCOH>2.0.CO;2.

——, and M. L. Weisman, 1996: Simulations of shallow supercell storms in landfalling hurricane environments. *Mon. Wea. Rev.*, **124**, 408–429, https://doi.org/10.1175/1520-0493(1996)124<0408:SOSSSI>2.0.CO;2.

——, and ——, 2001: The sensitivity of simulated supercell structure and intensity to variations in the shapes of environmental buoyancy and shear profiles. *Mon. Wea. Rev.*, **129**, 664–687, https://doi.org/10.1175/1520-0493(2001)129<0664:TSOSSS>2.0.CO;2.

Monin, A. S., and A. M. Obukhov, 1954: Basic laws of turbulent mixing in the atmosphere near the ground. *Tr. Akad. Nauk SSSR Geofiz. Inst.*, **24**, 163–187.

Morrison, H., J. A. Curry, and V. I. Khvorostyanov, 2005: A new double-moment microphysics parameterization for application in cloud and climate models. Part I: Description. *J. Atmos. Sci.*, **62**, 1665–1677, https://doi.org/10.1175/JAS3446.1.

Mullendore, G. L., 2019: Radar observations and simulations of the level of maximum detrainment in deep convection. *18th Conf. on Mesoscale Processes*, Savannah, GA, Amer. Meteor. Soc., 2.3, https://ams.confex.com/ams/18MESO/meetingapp.cgi/Paper/361266.

——, A. J. Homann, K. Bevers, and C. Schumacher, 2009: Radar reflectivity as a proxy for convective mass transport. *J. Geophys. Res.*, **114**, D16103, https://doi.org/10.1029/2008JD011431.

Murphy, T. A., and K. R. Knupp, 2013: An analysis of cold season supercell storms using the synthetic dual-Doppler technique. *Mon. Wea. Rev.*, **141**, 602–624, https://doi.org/10.1175/MWR-D-12-00035.1.

Naylor, J., and M. S. Gilmore, 2012: Convective initiation in an idealized cloud model using an updraft nudging technique. *Mon. Wea. Rev.*, **140**, 3699–3705, https://doi.org/10.1175/MWR-D-12-00163.1.

NWS Birmingham, 2016: Tornadoes of March 31, 2016. NWS, accessed 5 January 2017, https://www.weather.gov/bmx/event_03312016.

Orf, L., R. Wilhelmson, B. Lee, C. Finley, and A. Houston, 2017: Evolution of a long-track violent tornado within a simulated supercell. *Bull. Amer. Meteor. Soc.*, **98**, 45–68, https://doi.org/10.1175/BAMS-D-15-00073.1.

Peters, J. M., C. J. Nowotarski, and H. Morrison, 2019: The role of vertical wind shear in modulating maximum supercell updraft velocities. *J. Atmos. Sci.*, **76**, 3169–3189, https://doi.org/10.1175/JAS-D-19-0096.1.

Ripberger, J. T., C. L. Silva, H. C. Jenkins-Smith, D. E. Carlson, M. James, and K. G. Herron, 2014: False alarms and missed events: The impact and origins of perceived inaccuracy in tornado warning systems. *Risk Anal.*, **35**, 44–56, https://doi.org/10.1111/risa.12262.

Roberts, B., and M. Xue, 2017: The role of surface drag in mesocyclone intensification leading to tornadogenesis within an idealized supercell simulation. *J. Atmos. Sci.*, **74**, 3055–3077, https://doi.org/10.1175/JAS-D-16-0364.1.

——, ——, A. D. Schenkman, and D. T. Dawson II, 2016: The role of surface drag in tornadogenesis within an idealized supercell simulation. *J. Atmos. Sci.*, **73**, 3371–3395, https://doi.org/10.1175/JAS-D-15-0332.1.

Rotunno, R., and J. B. Klemp, 1982: The influence of the shear-induced pressure gradient on thunderstorm motion. *Mon. Wea. Rev.*, **110**, 136–151, https://doi.org/10.1175/1520-0493(1982)110<0136:TIOTSI>2.0.CO;2.

——, and ——, 1985: On the rotation and propagation of simulated supercell thunderstorms. *J. Atmos. Sci.*, **42**, 271–292, https://doi.org/10.1175/1520-0469(1985)042<0271:OTRAPO>2.0.CO;2.

Schenkman, A. D., M. Xue, and M. Hu, 2014: Tornadogenesis in a high-resolution simulation of the 8 May 2003 Oklahoma City supercell. *J. Atmos. Sci.*, **71**, 130–154, https://doi.org/10.1175/JAS-D-13-073.1.

Schneider, R. S., and A. R. Dean, 2008: A comprehensive 5-year severe storm environment climatology for the continental United States. *24th Conf. on Severe Local Storms*, Savannah, GA, Amer. Meteor. Soc., 16A.4, http://ams.confex.com/ams/24SLS/techprogram/paper_141748.htm.

——, ——, S. J. Weiss, and P. D. Bothwell, 2006: Analysis of estimated environments for 2004 and 2005 severe convective storm reports. *23rd Conf. on Severe Local Storms*, St. Louis, MO, Amer. Meteor. Soc., 3.5, http://ams.confex.com/ams/23SLS/techprogram/paper_115246.htm.

Sherburn, K. D., 2018: Environments and origins of low-level vortices within high-shear, low-CAPE convection. Ph.D. thesis, North Carolina State University, 212 pp.

——, and M. D. Parker, 2014: Climatology and ingredients of significant severe convection in high shear, low-CAPE environments. *Wea. Forecasting*, **29**, 854–877, https://doi.org/10.1175/WAF-D-13-00041.1.

——, and ——, 2019: The development of severe vortices within simulated high-shear, low-CAPE convection. *Mon. Wea. Rev.*, **147**, 2189–2216, https://doi.org/10.1175/MWR-D-18-0246.1.

——, ——, J. R. King, and G. M. Lackmann, 2016: Composite environments of severe and nonsevere high shear, low-CAPE convective events. *Wea. Forecasting*, **31**, 1899–1927, https://doi.org/10.1175/WAF-D-16-0086.1.

Simmons, K. M., and D. Sutter, 2009: False alarms, tornado warnings, and tornado casualties. *Wea. Climate Soc.*, **1**, 38–53, https://doi.org/10.1175/2009WCAS1005.1.

Smith, B. T., R. L. Thompson, J. S. Grams, A. R. Dean, and C. Broyles, 2012: Convective modes for significant severe thunderstorms in the contiguous United States. Part I: Storm classification and climatology. *Wea. Forecasting*, **27**, 1114–1135, https://doi.org/10.1175/WAF-D-11-00115.1.

Smith, T. L., S. G. Benjamin, J. M. Brown, S. Weygandt, T. Smirnova, and B. Schwartz, 2008: Convection forecasts from the hourly updated, 3-km High Resolution Rapid Refresh (HRRR) model. *24th Conf. on Severe Local Storms*, Savannah, GA, Amer. Meteor. Soc., 11.1, http://ams.confex.com/ams/pdfpapers/142055.pdf.

Thompson, R. L., R. Edwards, J. A. Hart, K. L. Elmore, and P. Markowski, 2003: Close proximity soundings within supercell environments obtained from the Rapid Update Cycle. *Wea. Forecasting*, **18**, 1243–1261, https://doi.org/10.1175/1520-0434(2003)018<1243:CPSWSE>2.0.CO;2.

Wagner, T. J., P. M. Klein, and D. D. Turner, 2019: A new generation of ground-based mobile platforms for active and passive profiling of the boundary layer. *Bull. Amer. Meteor. Soc.*, **100**, 137–153, https://doi.org/10.1175/BAMS-D-17-0165.1.

Weisman, M. L., and J. B. Klemp, 1982: The dependence of numerically simulated convective storms on vertical wind shear and buoyancy. *Mon. Wea. Rev.*, **110**, 504–520, https://doi.org/10.1175/1520-0493(1982)110<0504:TDONSC>2.0.CO;2.

——, and ——, 1984: The structure and classification of numerically simulated convective storms in directionally varying wind shears. *Mon. Wea. Rev.*, **112**, 2479–2498, https://doi.org/10.1175/1520-0493(1984)112<2479:TSACON>2.0.CO;2.

——, and R. Rotunno, 2000: The use of vertical wind shear versus helicity in interpreting supercell dynamics. *J. Atmos. Sci.*, **57**, 1452–1472, https://doi.org/10.1175/1520-0469(2000)057<1452:TUOVWS>2.0.CO;2.